Contents lists available at ScienceDirect

Biomedicine & Pharmacotherapy

Changes in chromatin accessibility and transcriptional landscape induced by HDAC inhibitors in TP53 mutated patient-derived colon cancer organoids

Teresa Gagliano [a],[1], Emanuela Kerschbamer [a],[1], Umberto Baccarani [a], Martina Minisini [a], Eros Di Giorgio [a], Emiliano Dalla [a], Christian X. Weichenberger [b], Vittorio Cherchi [c], Giovanni Terrosu [a], Claudio Brancolini [a],[*],[2]

[a] *Department of Medicine, Università degli Studi di Udine, Institute for Biomedicine, P.le Kolbe 4, Udine 33100, Italy*
[b] *Eurac Research, Institute for Biomedicine, Via Alessandro Volta 21, Bolzano 39100, Italy*
[c] *General Surgery Clinic and Liver Transplant Center, University-Hospital of Udine, Udine, Italy*

ARTICLE INFO

ABSTRACT

Here we present the generation and characterization of patient-derived organoids (PDOs) from colorectal cancer patients. PDOs derived from two patients with TP53 mutations were tested with two different HDAC inhibitors (SAHA and NKL54). Cell death induction, transcriptome, and chromatin accessibility changes were analyzed. HDACIs promote the upregulation of low expressed genes and the downregulation of highly expressed genes. A similar differential effect is observed at the level of chromatin accessibility. Only SAHA is a potent inducer of cell death, which is characterized by the upregulation of BH3-only genes *BIK* and *BMF*. Up-regulation of *BIK* is associated with increased accessibility in an intronic region that has enhancer properties. SAHA, but not NKL54, also causes downregulation of *BCL2L1* and decreases chromatin accessibility in three distinct regions of the *BCL2L1* locus. Both inhibitors upregulate the expression of innate immunity genes and members of the MHC family. In summary, our exploratory study indicates a mechanism of action for SAHA and demonstrate the low efficacy of NKL54 as a single agent for apoptosis induction, using two PDOs. These observations need to be validated in a larger cohort of PDOs.

1. Introduction

Cancers are complex entities composed of communities of different cell types. Cancer cells and cancer-associated cells are under the influence of the microenvironment and live in a three-dimensional (3D) tissue architecture [1]. Further complexity arises from the heterogeneity of cancer cells in terms of different genetically defined subpopulations that can dynamically expand or contract depending on the microenvironment and therapeutic interventions [2,3].

Colorectal cancer (CRC) is one of the most common malignancies, accounting for 10% of cancers diagnosed annually, and is the second leading cause of cancer-related deaths worldwide [4]. In early stages, standard therapy is surgery, and in advanced cases, adjuvant chemotherapy. Commonly used chemotherapeutic agents in CRC are 5-fluorouracil, oxaliplatin or irinotecan [5]. Unfortunately, approximately 30–50% of CRC patients relapse and die from the disease [4,6]. Therefore, validation of new therapeutic approaches for advanced CRC is urgently needed.

In recent years, culturing CRC cells derived from patients as organoids exhibiting a 3D epithelial structure compared to two-dimensional

  * Corresponding author.
  E-mail address: claudio.brancolini@uniud.it (C. Brancolini).
  [1] These authors equally contributed.
  [2] http://orcid.org/0000-0002-6597-5373

(2D) cell lines has provided better preclinical models to study the effects of drug treatments and to increase our knowledge of the tumorigenesis process. Furthermore, patient-derived organoids (PDOs) are seen as promising tools for drug sensitivity testing and personalized medicine [7–11].

Non-mutational genome reprogramming, achieved by epigenetic changes, is an important hallmark of cancer. Epigenetic reprogramming can also modulate the microenvironment [1]. Of particular interest is the possibility of reversing epigenetic reprogramming by selected inhibitors [12,13].

HDACs are important players in epigenetic reprogramming. In humans, HDACs comprise 18 different members belonging to different families and subfamilies [14]. The zinc-dependent HDACs have been intensively studied for the possibility of developing selective inhibitors [15]. HDACIs represent a heterogeneous class of molecules. First-generation HDACIs target the catalytic site without selectivity, whereas second-generation HDACIs can discriminate between different family members [16,17].

Much of our knowledge about the efficacy of HDACIs and the cellular responses they elicit comes from cancer cell lines studied in 2D culture models. Unfortunately, with few exceptions, the promising efficacy in preclinical models has not been confirmed by clinical studies [15,18]. Of current interest is the evaluation of HDACIs as part of combinatory regimens [15,19]. In preclinical models, the efficacy of epigenetic therapy based on HDACIs in affecting the action of immune cells, has been demonstrated even in the case of metastasis [20,21].

In the present manuscript, we describe the generation of PDOs from various CRC patients and characterize their mutational burden. Next, we used PDOs from patients with advanced CRC carrying TP53 mutations to compare a nonselective (SAHA) and a selective (NKL54) class I HDAC inhibitor in terms of antiproliferative effect, genomic reorganization, and transcriptomic adaptations.

2. Materials and methods

2.1. Human tissues

Tissues were obtained from the struttura organizzativa complessa of Surgery at the University Hospital "Santa Maria della Misericordia" (Udine, Italy). After surgical removal, a portion of each colon tumor and the adjacent normal tissue was immediately frozen for storage and further uses. In parallel, a portion of the cancer tissue was used to prepare PDOs. This study was approved by the Comitato Etico Unico Regionale, (ID 3227–22/05/2020). The informed consent was obtained before sample collection. The tissue acquisition was accomplished during 2021–22. This study was performed in accordance with the Declaration of Helsinki.

2.2. Establishment of patient-derived organoids

Tissues from surgery were washed gently with cold 1X PBS for at least 3 times and were mechanically cut into ~0.5×1–1×1 mm^3 pieces using a sterile surgical blade in a 100 mm petri dish (Sarstedt). At least 2 pieces of the samples were immediately frozen in liquid nitrogen for further analysis. The remaining pieces were then suspended in DMEM/F12 medium containing 0.05 mg/ml Liberase TM (Roche) and 10 μM Y-27632 (Sigma) and 100 μg/ml Primocin (InVivoGen). Incubation with enzymes was performed in orbital shaker-incubator at 37°C for 15 minutes. After digestion, dissociated tissues were passed through a 40-μm cell strainer (Corning). Cell suspension was then centrifuged at 400 g for 5 min at 4°C and then re-suspended with BME (ultimatrix, biotechne) and seeded in 24-well plates (30 μL BME/well). The plates were then incubated for 20 minutes at 37°C before adding DMEM/F12 advanced medium (DMEM/F12 (Gibco), 100 U/ml penicillin/streptomycin (Gibco), Primocin (InvivoGen), 2 mM GlutaMAX (Gibco), 1x B27 (Gibco), 100 nM prostaglandin E2 (Tocris), 0.5 μg/ml R-spondin

(Peprotech), 4 mM nicotinamide (Sigma), 10 nM gastrin I (Sigma), 50 ng/ml EGF (Peprotech), 100 ng/ml Noggin (Peprotech)). Medium was changed every 3 days.

2.3. Organoids drug treatments and proliferative analysis

Cell viability was evaluated by the 3D Cell Titer GLO (Promega) following manufacturer instruction. Cells were seeding 2×10^4 cells/well in 10 μl of BME, in 96-well black plates (Sarstedt) as previously described [22] and treated with the indicated compounds for the indicated time points. Control cells were treated with vehicle alone (0.1% DMSO). After incubation, the revealing solution was added, and the luminescent output (relative luminescence units, RLU) was recorded using the Modulus plate reader (Promega). Results are expressed as mean value ± standard error of the mean (SEM) percent relative light units (RLU) vs. vehicle-treated control cells from 3 independent experiments in 6 replicates.

2.4. Lipophilic tracer staining and confocal microscopy

DiOC6(3) (Thermofisher) was added to 10^6 cells in serum-free medium to a final concentration of 1 μM. Cells were then incubated at 37°C for 1 h and centrifuged for 5 minutes at 300xg and washed twice with PBS. Finally, cells were resuspended in fresh complete medium and used for further assays. Organoids stained with lipophilic tracer and treated with indicated compounds were imaged using a 20X objective, SP8 Leica microscope (Leica Microsystems), equipped with a stage top incubator controlling temperature, CO_2 and humidity (Okolab), every 60 minutes for 72 hours. Image analysis was performed using the Leica Acquired Software X (LASX). Fluorescence intensity/time ratio was calculated after drawing a region around the PDO (region of interest; ROI) and measuring its mean fluorescence Intensity (PDO_{MIF}). The fluorescence of the background (BAC_{MIF}), which is from another ROI located in a non-fluorescent region, was subtracted from the PDO_{MIF} and the obtained value was multiplied by the area of the PDO.

For immunofluorescence PDOs were seeded in μ-Slide 8 Well Glass Bottom (#80807, Ibidi), and allowed to settle and grow for 72 hours. PDOs were then fixed with 3% paraformaldehyde, permeabilized with 0.2% Triton X-100 and blocked with 0.1% BSA. After blocking, primary antibodies (E-Cadherin, Ki-67, Cell Signalling) were added to the wells. Cells were then incubated with secondary antibodies (Alexa Fluor 488 or Alexa Fluor 546, Thermofisher), Hoechst and Phalloidin 546 (Thermofisher). Afterwards slides were imaged using SP8 Leica microscope.

2.5. Caspase assay

The caspase activity was evaluated using the Apo-ONE caspase-3/7 homogeneous assay (Promega). Briefly, organoids were seeded as described above, and treated with the indicated compounds for 24 or 48 hours. Control cells were treated with vehicle alone (0.1% DMSO). Results are expressed as mean value ± SEM percent RLU vs. vehicle-treated control cells from three independent experiments in three replicates.

2.6. HDAC assay

HDAC activity was measured using HDAC GLO I/II assay (Promega), following manufacturer instruction as previously describe [23]. Briefly, organoids were seeded in 96 well plates as described above. Samples were treated with increasing concentration of HDACs inhibitors for 6 hours. After incubation time, 50 μl of working solution, containing HDAC-Glo buffer and substrate, was added to each well. The plate was then incubated at room temperature for 45 minutes, and then read using modulus microplate reader (Promega). Results are expressed as mean value ± SEM percent RLU vs. vehicle-treated control cells from three independent experiments in 2 replicates.

2.7. Genomic analysis

Genomic DNA was extracted from organoids, tumors, and adjacent normal tissues using DNA Investigator kit (Qiagen). DNA concentration and quality was evaluated using capillary electrophoresis on Bioanalyzer (Agilent). Whole-exome sequencing (WES) was performed using the Illumina Novaseq platform (GENEWIZ). We used the FastQC tool (v0.11.8) (https://www.bioinformatics.babraham.ac.uk/projects/fastqc) to evaluate the quality of fastq files and summarized the output with multiQC (ver1.4) [24]. We used the Burrows-Wheeler Aligner (BWA) to align reads to the NCBI GRCh38 human genome reference assembly. We used Samtools [25] and Picard (https://broadinstitute.github.io/picard) for data conversion, indexing and manipulation. We called somatic single nucleotide variants (SNVs), insertions and deletions (indels) through local assembly of haplotypes as per the GATK somatic short mutation calling best practice workflow (https://gatk.broadinstitute.org/hc/en-us/articles/360035531132), using the Mutect2 method [26] on paired tumor/normal samples and applying the recommended settings. We annotated the variants that passed the filtering steps using the ANNOVAR software tool. Specifically, we retained those deemed deleterious according to SIFT or CLINVAR and those with an undefined role that were non-synonymous and mapped to gene exons, splicing junctions or UTRs. Finally, we used bcftools to extract variant statistics and plot the summarized results [27]. Non-synonymous somatic mutations were defined as follows: firstly, we selected the mutations that appeared within the consensus coding sequence region designed by the CDS project; secondly, we removed variants with variant count <3, allele frequency <5% or total depth <25; lastly, we filtered out synonymous and splice region mutations, retaining only non-synonymous mutations (missense, nonsense, insertions and deletions mutations). We filtered VCF files to exclude silent variants or variants called in introns. MutationalPatterns (v3.10) was used to gather and plot point mutation frequencies [28].

2.8. RNA extraction and RNA-seq analysis

Total RNA was extracted from the organoids treated with the two HDACIs using PureLink RNA Mini Kit (Invitrogen) following the manufacturer's instructions. RNA concentration and quality was evaluated using capillary electrophoresis on Bioanalyzer (Agilent). cDNA libraries were generated from poly(A) selected RNA and 150 bp paired end sequencing was performed by Biodiversa (Treviso, Italy). Data analysis was carried out as previously described [23]. Briefly, (FastQC (v0.11.9) and MultiQC (v1.14) were used to inspect raw reads, all samples passed the quality controls. Illumina universal adapters were removed with fastx_clipper from FastQC. Transcripts were quantified with salmon (v1.4.0) on human transcriptome GRCh38. Transcript quantifications were summarized at the gene level after being imported into the R statistical language (v4.3) through Bioconductor (v3.17) package tximeta (v1.18.1) [29]. Principal component analysis on the 5000 most variable genes was run with the plotPCA function from the DESeq2 package (v1.40.2). We removed genes with raw counts mean <10 between each condition replicates from the analysis. Differential expression analysis was performed using DESeq2 with Wald test for significance. Adjustment for multiple hypothesis testing was carried out by Benjamini-Hochberg correction at a false discovery rate (FDR) of 0.05. Genes reported significantly by DESeq2 with an absolute $\log_2$ (fold change) > 1 were considered as differentially expressed. The packages AnnotationHub (v3.8.0) and ensembldb (v2.24.0) were used to annotate genes with Ensembl annotation version 107 [30]. Functional annotation was performed on KEGG, Reactome and Gene Ontology databases with ClusterProfiler (v4.8.3) and ReactomePA (v1.44.0), respectively [31]. GO term and pathway analysis results are reported at a significance level of 0.05 (p value).

2.9. ATAC-seq and analysis

Organoids were treated with NKL54 10 μM, SAHA 5 μM, and vehicle only (DMSO). After 6 hours of treatment cells were collected and counted. At least 1 million of live cells for each condition were frozen in FBS 10% DMSO and shipped in dry ice to Biodiversa (Treviso, Italy) to perform ATACseq. Data were analyzed using the Nextflow (v21.10.4) nf-core atacseq pipeline (v1.2.1) for the preliminary steps, alignment on GRCh38 and peak calling [32]. Peaks called by MACS2 (v2.2.7.1) within the nf-core pipeline, were loaded in R and normalized using the library size as reads in peaks (libRiP) normalization within DiffBind. The normalization factors for each sample were used in deepTools, bamCoverage to produce bigwig files for computeMatrix and plotHeatmap in order to plot the ATAC reads distribution on the trascriptional start sites of all genes [33]. Clustering was done by plotHeatmap kmeans based on the control samples only. Differentially enriched regions were calculated starting from a list of 64856 consensus peaks obtained by a minimum overlap of 2 between all samples. All SAHA against all control samples were compared by DiffBind with DESeq2 method, regions were considered differential with FDR < 0.05. Differentially enriched regions were annotated with ChIPseeker (v1.36.0) on hg38 genomic regions [34]. Motifs enrichment analysis was run on enriched or depleted regions with SEA (online, v5.5.4) of the MEME suite using shuffled input sequences as background, on JASPAR Vertebrates and UniPROBE Mouse databases [35]. Transcription factor binding motifs in single ATAC peaks were searched with Motif Occurrence Detection Suite (MOODS) (v1.9.4) with p value threshold of 10^{-7} on the JASPAR core matrices [36].

2.10. Statistical analysis

Comparison of biological assays was performed using one-way Anova and Tukey's multiple comparisons tests. Data were analyzed using GraphPad (Prism v-9.0) and results reported with P values <0.05 were considered significant (*).

3. Results

3.1. Genomic characterization of CRC and CRC-derived organoids

PDOs were derived from surgically resected tissue from untreated CRC patients (Fig. 1A, Table S1). Genomic DNA was isolated from the tumor and corresponding normal tissue and subjected to whole-exome sequencing (WES) to characterize the different patients for tumor-specific patterns of somatic mutations. The tumors were from 4 different patients (P10, P13, P19 and P71). As previously reported for CRC [7], C-to-T transitions were the most common mutations (Fig. 1B). Next, we analyzed the pattern of somatic mutations in the different patients. We selected two different gene groups to represent the mutation status using a heatmap: i) the most frequently mutated genes in CRC (n = 614), including genes with a mutation frequency of up to 5.6% in CRC as reported by TCGA (Table S2), and ii) the most frequently mutated cancer genes (CG, n = 636), consisting of driver genes with a mutation frequency of up to 1.7%, as reported by TCGA (Table S2). There exists a small overlap between the two gene sets.

Analysis of somatic mutations in the CRC genes shows that each patient has a unique mutation pattern (Fig. 1C and Table S3), with missense mutations being the most common. *APC* is mutated in all patients, *TP53* is mutated in P19 and P71 (p.Q192* and p.C135F, respectively), while *KRAS* is mutated in P10 and P71 (respectively p.G13D and p.G12D). Notably, both *TP53* mutations are relatively rare in CRC (https://tp53.isb-cgc.org/search_gene_by_var).

Analysis of the CG mutations also revealed a specific mutation pattern in each patient, with different proto-oncogenes and tumor suppressors involved (Fig. 1D, Table S3). Interestingly, the different mutated CGs are representative of common gene ontology categories, specifically receptor tyrosine kinase signaling, transcription, and
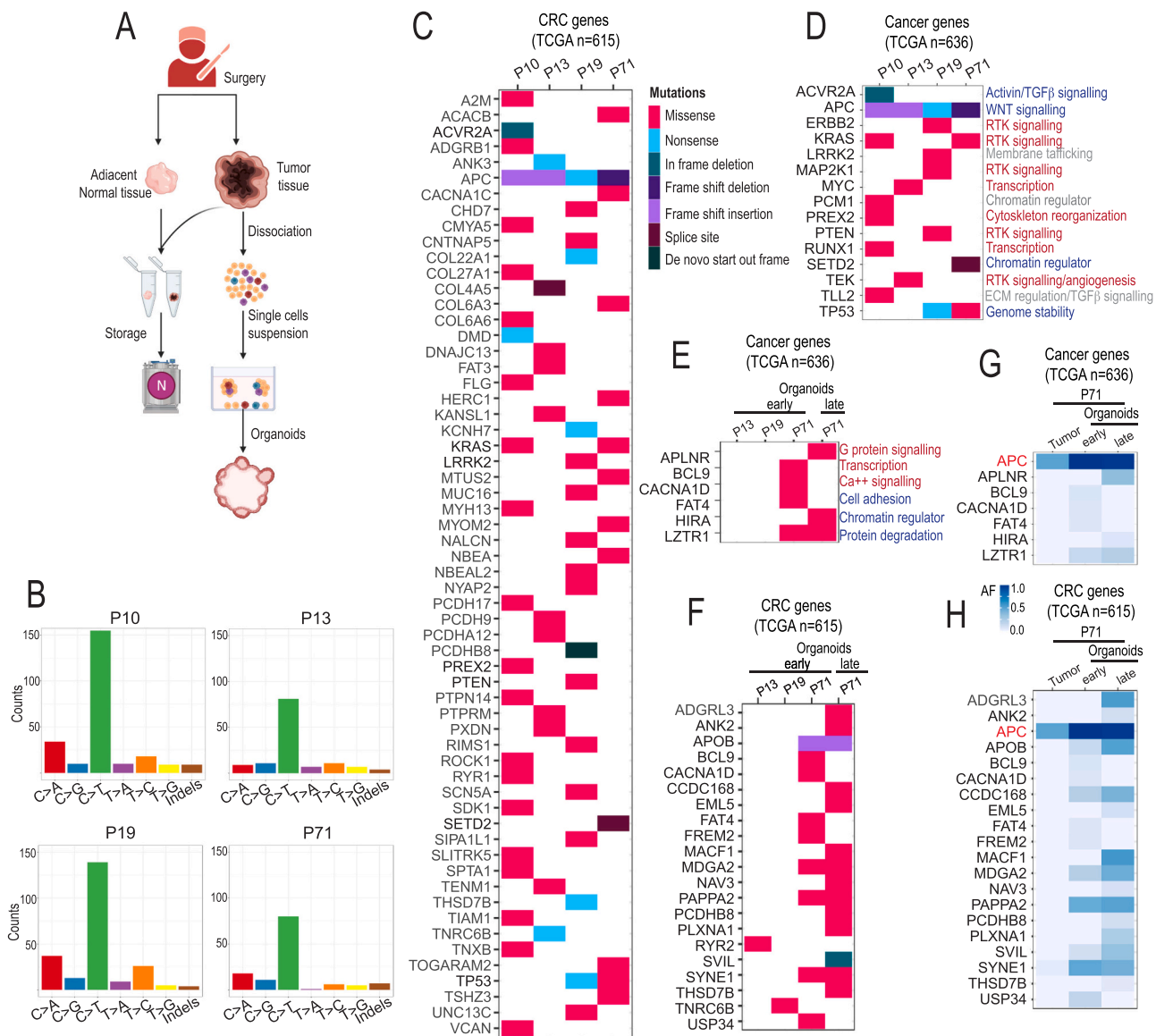
Fig. 1. Definition of the mutational status of CRC patients and of derived PDOs. A. Workflow of the procedure to establish PDOs from CRC patients. Tumors and adjacent normal tissues were also isolated to purify DNA and to establish the mutational status. For patient characteristics, see Table S1. B. Bar plot representing the number of single nucleotides substitution and small insertions and deletions (indels) detected in the four CRC patients. C. Heatmap showing the mutation status of the 614 most frequently mutated CRC genes in the four patients compared to the matched normal tissues. D. Heatmap showing the mutation status of the 636 most frequently mutated cancer driver genes (CGs) in the four patients compared to the matched normal tissues. E. Heatmap showing the mutation status of the 636 most frequently mutated cancer driver genes (CGs) in the 3 PDOs compared to the matched original tumor. For POD71 WES was also performed after 16 passages in culture. F. Heatmap showing the mutation status of the 614 most frequently mutated CRC genes in the 3 PDOs compared to the matched original tumor. For POD71 WES was additionally performed after several passages in culture (n=16). G. Heatmap showing the allele frequency (AF) of mutations in the indicated drivers CGs in tumor of patient P71 the relative PDO, at early and late passages with respect to the matched normal tissue. APC (in red) was used as a reference, H. Heatmap showing the allele frequency of mutations in the indicated drivers CRC genes in tumor of patient P71 the relative PDO, at early and late passages with respect to the matched normal tissue. APC (in red) was used as a reference, Only mutated genes are shown. For CGs oncogenes are in red, tumor suppressors in blue. Undefined roles are in gray. The main gene function is described.

chromatin regulation.

To avoid competition between normal organoids and tumor organoids, cultures were established in the absence of WNT factors and RSPO1. Under this condition, the expansion of cells carrying mutations in *APC* or other alterations supporting the WNT signaling pathway is favored [7]. We obtained organoids from P13, P19, and P71. We have never observed the growth of cells from P10. WES was performed for these 3 PDOs. The cultured PDOs from P13 and P19 had the same mutation pattern for the cancer driver genes (CG) as the primary tumors (Fig. 1E, Table S3). This stability was confirmed when the analysis was extended to the CRC genes (Fig. 1F, Table S3). In contrast, PDOs from

P71 feature the appearance of new mutations in CGs (Fig. 1E, Table S3), a condition that was confirmed by analysis of the CRC genes (Fig. 1F, Table S3).

To monitor the evolution of the mutational load in PDOs of P71, WES was also performed after 16 passages in culture (late passages). Analysis of the mutation status of the CG and CRC genes confirmed the tendency for new mutations to accumulate (Table S3). The appearance of new mutations could be due to Darwinian selection of certain subclones during the culture of PDOs. These subclones could already have been present in the original tumor. In addition, the growth of PDOs in culture could contribute to the acquisition of new mutations [37]. To address

these possibilities, we analyzed the frequency of mutations in tumor and PDOs at early and late passages for both the CG (Fig. 1G, Tables S3 and S4) and CRC genes (Fig. 1H, Tables S3 and S4). Mutation frequency of *APC*, used as a reference, increases during culturing of PDOs, indicating positive selection for cancer cells, as expected from the culture conditions. For some driver mutations, the frequency increases from early to late passages (*HIRA, LZTR1, APLNR*), while others disappear (*BCL9, CACNA1D, FAT4*). This analysis suggests that subclone selection is an important source of mutation consolidation, but we cannot exclude the possibility that the growth of PDOs in culture favors the appearance of some new mutations.

3.2. Evaluation of different HDAC inhibitors on the growth of CRC organoids

PDOs are useful tools for screening effective drug treatments in relation to the specific mutation status of patients. TP53 mutations are associated with lower efficacy of classical chemotherapeutic treatments and lower overall survival of CRC patients [38–40]. Therefore, the PDOs of P19 and P71 carrying TP53 mutations were further investigated to evaluate alternative drug treatments.

These two PDOs are characterized by different morphologies. PDO19 exhibit smooth margins and a compact morphology, whereas aggregated shapes are more common in PDO71, often resulting in irregular margins (Fig. 2A).

Confocal images and F-actin staining showed that both PDOs maintain an epithelial structure with a lumen and normal polarity [41]. Both PDOs are characterized by a high percentage of cycling cells, as evidenced by the Ki67-positive cells (Fig. 2B). The percentage of Ki67-positive cells was similar in both PDOs (Fig. 2C).

HDACIs are used in the clinic for certain hematologic malignancies, but they show low efficacy in solid tumors [15]. However, their use in combination with other drugs or treatments could provide additional therapeutic benefits in a rational design and is currently under investigation [42–45]. Furthermore, after the initial discovery of pan-HDACIs, more selective subclass-specific inhibitors have been developed [15]. Here, we compared, as single agents, the activity of a nonselective HDACIs such as SAHA/vorinostat, which also has additional targets [46] and of the HDAC1/2/3 specific inhibitor, NKL54 [23].

To examine the effect of the two HDACIs, at the level of growth of individual PDOs, we used time-lapse confocal microscopy. To monitor cell growth/survival, we used the cationic dye DiOC6(3), which accumulates in mitochondria due to mitochondrial membrane potential but also stains intracellular membranes of the endoplasmic reticulum [47]. Subsequently, individual PDOs were observed over time by confocal microscopy and fluorescence intensity was measured (Fig. 2D). Untreated PDOs show a heterogeneous pattern of fluorescence intensity over time. In some PDOs, fluorescence increases sharply (especially in PDO71), possibly indicating strong cell proliferation. Other PDOs show constant fluorescence or a slight decrease. We initially used a concentration of the two HDACIs derived from previous studies in 2D cultures [23] and verified in CRC cell lines (Fig. S1). In the presence of SAHA, the fluorescence of PDOs gradually decreases in several organoids, possibly indicating the occurrence of some cell death. In fact, membrane disruption causes le loss of fluorescence. In the presence of NKL54, the fluorescence of PDOs does not increase excessively, but they also do not show a dramatic decrease in DiOC6(3) staining, ruling out the induction of overt cell death.

To better demonstrate the differential effect of SAHA and NKL54 on PDOs viability, we used a luminescence assay to measure PDOs viability. Dose-dependent studies showed that SAHA strongly affected PDOs viability in both patients, whereas NKL54 was relatively ineffective (Fig. 2E).

Because HDACIs are known to induce apoptosis, the activities of the executor caspases (caspase-3 and caspase-7) were examined using the DEVDase assay. Analysis was performed at 24 and 48 hours (Fig. 2F).

SAHA induced caspase activity in PDOs of both patients to a high extent, with higher levels at 24 hours after treatment. As expected, NKL54 hardly induced caspase activation.

The profound difference exerted by the two inhibitors on PDOs survival might be due to the different efficacy of inhibition of the different HDACs expressed in PDOs. Therefore, we decided to directly compare the inhibitory effects of SAHA and NKL54 in PDOs. Dose-dependent studies demonstrated that SAHA inhibits the activities of class I and IIb HDACs to a high extent (Fig. 2G). In contrast, NKL54 only modestly inhibits class I and IIb HDACs activities. Therefore, the different effect of the two inhibitors on the two PDOs survival might depend on the different potency of inhibition or the different pattern of inhibited HDACs.

3.3. Transcriptomic adaptations in PDOs after SAHA and NKL54 treatments

To investigate the cellular responses induced by the two HDACIs in the two PDOs, RNA-seq experiments were performed. The two PDOs were treated with 5 μM SAHA or with 10 μM NKL54 for 6 hours. Principal component analysis (PCA) shows the high reproducibility of the three biological replicates (Fig. S2A). The two PDOs are characterized by a different transcriptomic profile. In addition, PCA reveals that NKL54 is very similar to DMSO-treated PDOs, suggesting a weak effect on gene expression. We next analyzed the expression levels of the different zinc-dependent HDACs between the two patients (Fig. 3A). In class I, HDAC1 and HDAC2 are the most highly expressed. In class IIa, HDAC7 shows the highest amount of mRNA copies. Class IIb HDAC6 and HDAC10 are expressed at similar levels. Overall, the pattern of zinc-dependent HDACs expression is similar among the two PDOs.

Previous studies have shown that HDACIs cause upregulation of weakly expressed genes and downregulation of highly expressed genes, as part of a compensatory effect [23,48]. Analysis of gene expression in TPM (transcript per million) confirmed that SAHA and NKL54 similarly affect the expression of low- and high-abundance mRNAs in both PDOs (Fig. 3B).

We next analyzed differentially expressed genes (DEGs) in response to HDACIs in the two PDOs. Genes that are upregulated in response to SAHA are the same in a high percentage in both PDOs (72% in PDO19 and 80% for PDO71) (Fig. 3C, top). In contrast, a much smaller number of genes is upregulated by NKL54 compared to SAHA, and these genes are largely distinct between the two PDOs (only 43% and 51% for PDO19 and PDO71, respectively) (Fig. 3C, bottom, Table S5). A similar trend was observed for the downregulated genes (Fig. S2B, Table S5).

We next analyzed the correlations between the two inhibitors. Several genes upregulated by NKL54 are identical to SAHA (62% for PDO19 and 57% for PDO71). In general, only a few genes are downregulated by NKL54 in both patients, and only a few of them are in common with SAHA (Figure S2C).

Among class I HDACs, HDAC1, 2, and 3 are more efficiently inhibited by NKL54 [23]. Therefore, among the genes upregulated by both SAHA and NKL54, the targets of these HDACs should be found as common regulated genes. We have shown that NKL54 is much less effective in inhibiting HDAC activities in PDOs compared to SAHA (Fig. 2G). Consequently, and confirming this observation, we should see less upregulation of these common genes in PDOs treated with NKL54 than in SAHA. Fig. 3E shows that these common genes are indeed more upregulated in the presence of SAHA. The plots in Figs. 3F and S2D confirm that the levels of mRNAs upregulated by both SAHA and NKL54 (pink dots) are much higher in PDOs treated with SAHA, with few exceptions.

These data confirm that NKL54 is a less potent inhibitor of HDAC1/2/3 compared to SAHA in the two PDOs analyzed.
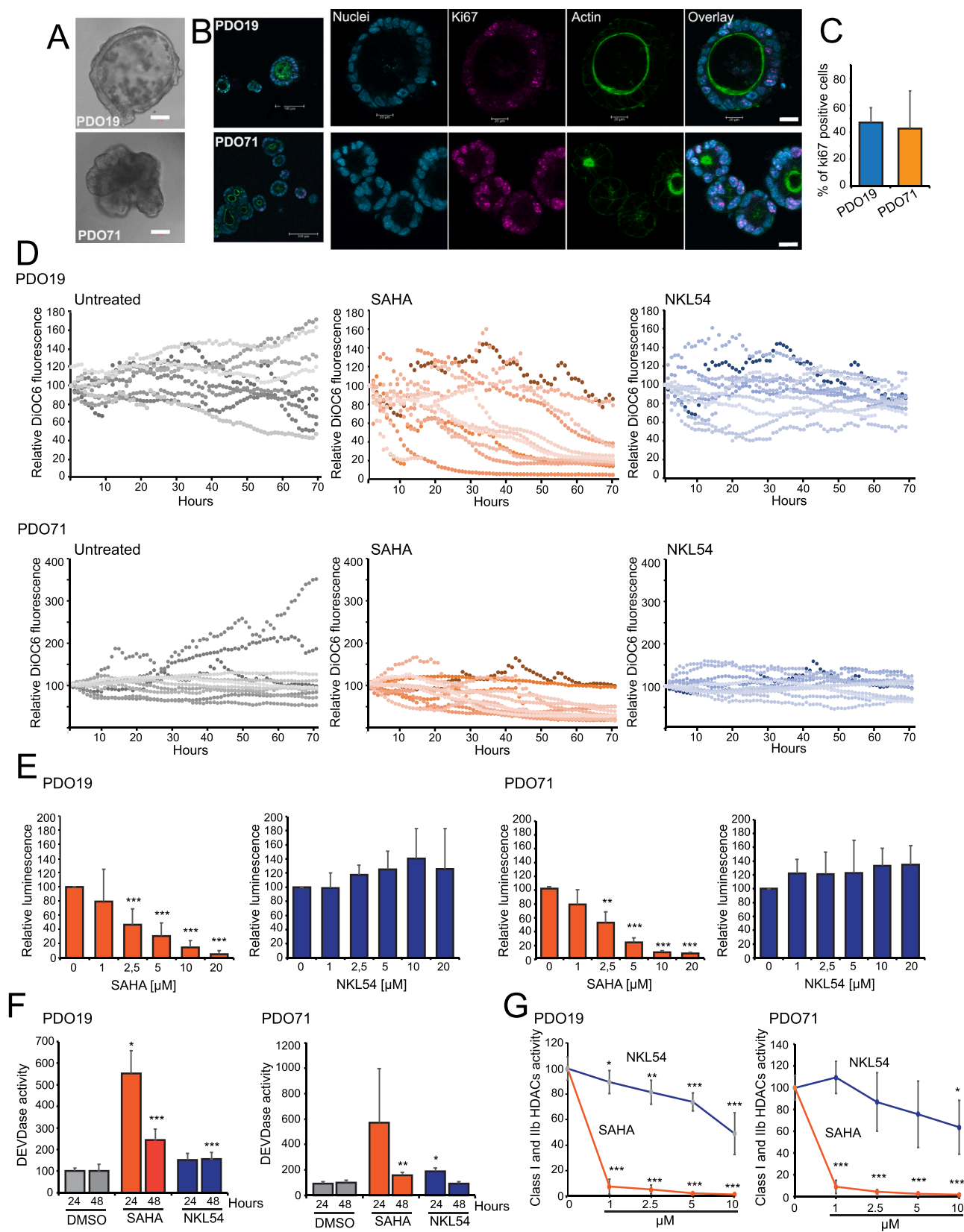
(caption on next page)

Fig. 2. Effects of HDACIs on PDO19 and PDO71 proliferation and apoptosis. A. Brightfield images of PD019 and PDO71 acquired with confocal microscope. B. PDO19 and PDO71 stained with Hoechst (blue, nuclei) Ki67 (magenta) and actin (green). C. Percentage of Ki67 positive nuclei/PDOs. D. 72 hours time-lapse analysis of relative fluorescence of PDO19 and PDO71 treated with vehicle only, SAHA 5 μM or NKL54 10 μM. Each line represents a single organoid. Cells were labelled with the DiOC6(3) at a concentration (1 μM), that allow the staining of the endoplasmic reticulum [93]. Fluorescence intensity is directly correlated with cell viability, decreasing in cell viability results in lower fluorescence intensity, E. Cell viability of PDO19 and PDO71 was measured after 72 hours of treatment with increasing dose of SAHA ore NKL54. Significance was calculated using one-way Anova and Tukey's multiple comparisons tests. Results are expressed as mean $\pm$SD; ** P < 0.01, *** P < 0.001 vs vehicle treated cells. F. Caspase 3/7 activity of PDO19 and PDO71 treated with SAHA 5 μM or NKL54 10 μM measured after 24 and 48 hours. Significance was calculated using one-way Anova and Tukey's multiple comparisons tests. Results are expressed as mean $\pm$SD; *P < 0.01, ** P < 0.0001, *** P < 0.001 vs vehicle treated cells. G. Class I and IIb HDACs activity was assess in PDO19 and PDO71 treated with increasing concentrations of SAHA and NLK54. Significance was calculated using one-way Anova and Tukey's multiple comparisons tests. Results are expressed as mean $\pm$SD; *P < 0.01, ** P < 0.0001, *** P < 0.001 vs vehicle treated cells.

3.4. Genes and pathways induced by SAHA and NKL54 in PDOs

Gene set analysis (GSA) was applied to elucidate the pathways and functions of genes upregulated by the two HDACIs. First, we analyzed the core of common genes, considering the two HDACIs and the two PDOs as duplicates (Fig. S3E, Table S5). These genes are enriched in categories related to neurogenesis and adhesion (Fig. 3G, Table S6), as observed in other transcriptomic characterizations of cellular responses to HDACIs [23,49,50].

Subsequently, the genes upregulated by each inhibitor in each PDOs were analyzed independently. SAHA elicited similar responses in both PDOs, with the microtubule dynamics and axoneme organization categories being the most enriched (Fig. 3H, Table S7 and S8). A different scenario is observed for NKL54. In PDO19, the most enriched category is related to the immune response, with genes of the class II major histocompatibility complex (MHC) (Fig. 3I, Table S9). In contrast, genes of the innate immune system category are the most enriched in PDO71 (Table S10).

In summary, SAHA and NKL54 differ in terms of effects on gene transcription and SAHA elicits almost homogeneous responses in the two PDOs, whereas patient-specific effects predominate in NKL54.

3.5. Cell cycle and apoptotic genes are differentially affected by SAHA and NKL54

One of the main differences between SAHA and NKL54 is the effect on cell survival and proliferation profile of PDOs. It is known that HDACIs can promote the expression of cyclin-dependent kinase inhibitors (CDKIs), particularly *CDKN1A*, and BH3-only pro-apoptotic members of the BCL2 family [51,52]

Therefore, we first compared the effects of HDACIs on CDK inhibitors, with SAHA affecting multiple CDKIs (Fig. 4A). In addition to *p21/CDKN1A*, it also upregulates *p15/INK4b/CDKN2B* and *p19/INK4D/CDKN2D*, as observed previously [53,54]. These effects were even more pronounced in PDO19. Surprisingly, NKL54 did not affect *CDKN1A* expression and only increased, albeit to a lesser extent, mRNA levels of *p15/INK4b/CDKN2B*. In contrast, mRNA levels of *p27/KIP1/CDKN1B* were reduced in both PDOs in response to both HDACIs.

Even more striking was the differential effect of the two inhibitors on the expression of BCL2 family members (Fig. 4B). SAHA induced the upregulation of several BH3-only genes (*BIM*, *BMF*, and *BIK*) with a concomitant strong downregulation of the anti-apoptotic *BCL2L1*. Again, the effect was more pronounced in PDO19. The effect of NKL54 was modest, leading only to a marked increase in *BMF* mRNA.

3.6. Genes of the immune response are similarly influenced by SAHA and NKL54

Overall, our studies suggest that the pan-HDACI SAHA has a potent inhibitory effect and stronger effects on gene expression than the class I inhibitor NKL54. However, it is interesting to note the induction of immune-related genes by NKL54, such as MHC class II genes (Fig. 3I). Indeed, HDACIs are currently being tested in clinical trials as potentiators of the immune response. Previous studies have shown that HDACIs

can upregulate the expression of members of the MHC II [55] and the enhancement of the anti-tumor activity of the immune system [56–58]. This inspired us to analyze the expression levels of HLA genes in detail.

HLA-DMA and *HLA-DMB* were induced by both inhibitors, surprisingly much stronger by NKL54, and the effect was patient-specific (Fig. 4C). *HLA-DBO* and *HLA-DRB5* upregulation was specific for NKL54 in PDO19. In contrast, upregulation of *HLA-DQB1* was restricted to SAHA, but both PDOs responded. To obtain a complete picture of HLA status, we extended the analysis to MHC class I genes (Fig. 4D). SAHA promoted the upregulation of *HLA-B*, *HLA-F* and of the HLA-related *MICA*, only suppressing the expression of *HLA-H*. NKL54, apart from *HLA-F*, was much less effective compared with SAHA. These results and the patient-specific responses should be validated in a larger cohort of PDOs.

GSA showed that innate immunity genes were also upregulated in response to NKL54 (Fig. 3I). Therefore, to better clarify these aspects, the expression levels of enriched genes belonging to the Reactome category "diseases of the immune system" (Table S9) were analyzed in more detail (Fig. 4E). Some of these genes are upregulated in response to the two inhibitors in both PDOs (*CD14, FGA, FGB*), but TLRs responded stronger to treatment with NKL54, demonstrating another difference between the two inhibitors.

In the colon, class II MHC molecules are mainly expressed by professional antigen-presenting cells (APCs) such as dendritic cells, macrophages, and B cells, but also by nonprofessional APCs such as epithelial and mesenchymal cells [59]. The upregulation of certain MHC class II genes prompted us to assess their overall expression levels. In the TPM (Transcripts per million) plot (Fig. 4F) we see that, except for *HLA-DQB*, *HLA-DRB1* and *HLA-DRB5*, MHC II are very low-expressed genes. In contrast, MHC class I genes *HLA-A* and *HLA-C* are much more highly expressed (Fig. 4G) and belong to the category of moderately highly expressed genes [60].

3.7. Analysis of chromatin accessibility in PDOs after SAHA and NKL54 treatments

Next, we analyzed the changes in chromatin accessibility, as induced by the two HDACIs in PDOs, using ATAC-seq. PCA shows good reproducibility of the two biological replicates (Fig. S3A). As with the RNA-seq data, the differences between the two PDOs were more pronounced with respect to the response to treatments. Since active transcription start sites (TSS) are frequently found in open chromatin [61], we initially analyzed the ATAC-seq signals at TSS. Four different clusters can be recognized based on the intensity and the spreading of the ATAC-seq signal around the TSS. Cluster 1 is characterized by highly accessible chromatin (Fig. 5A). Within this category we found 2176 genes and some of them are highly expressed (Fig. 5B). The most enriched GO categories are protein folding and chaperons (Table S11). Cluster 2 groups TSS that show a more diffuse ATAC-seq signal around the TSS. Here the most enriched GO categories are ribonucleoprotein complex biogenesis and mitochondrial matrix (Table S12). Cluster 3 resemble cluster 1 although the ATAC-seq signals are less intense and accordingly genes are, on average, less expressed. The most enriched GO categories are cell adhesion and histone modification (Table S13).
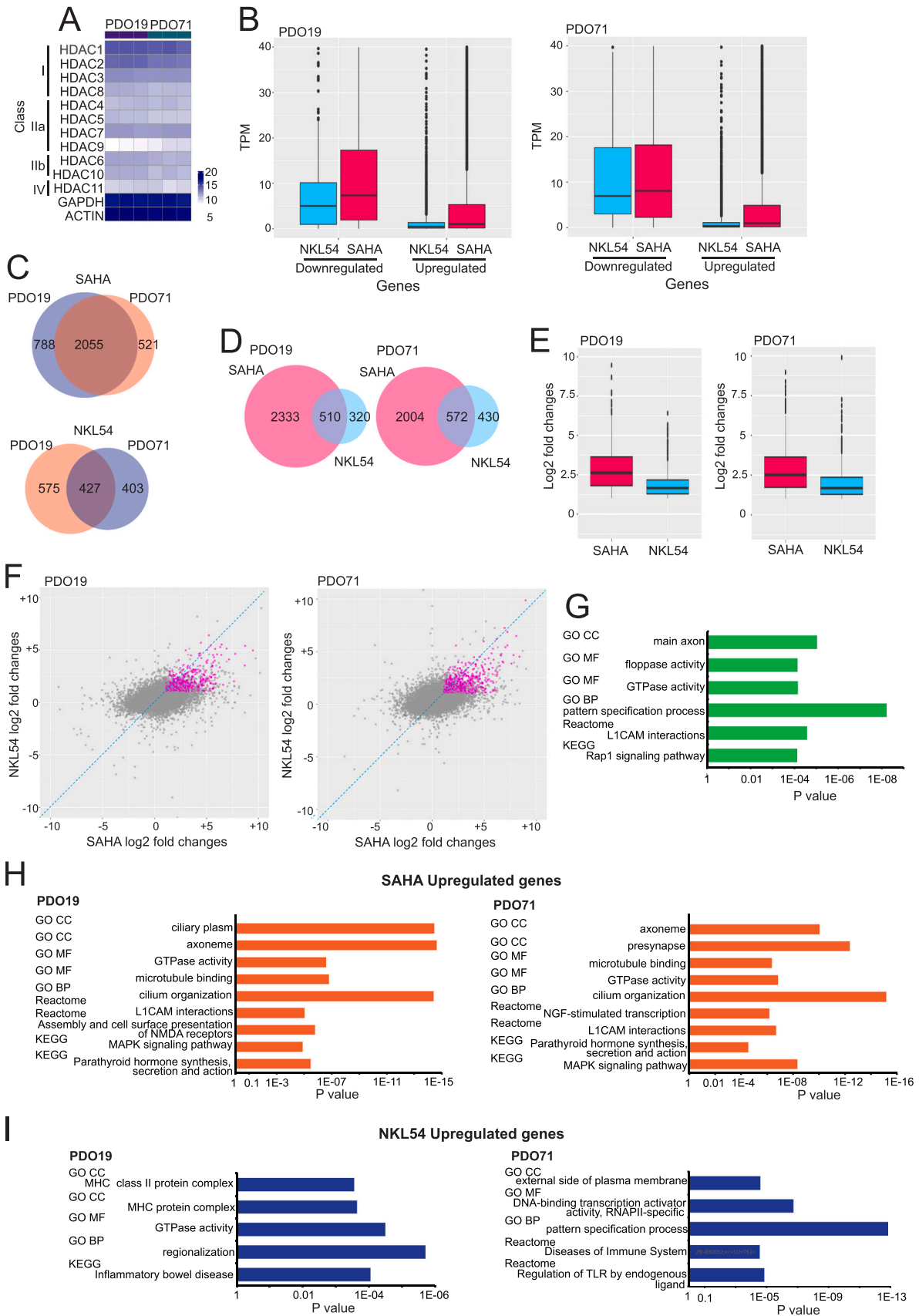
(caption on next page)

Fig. 3. Transcriptomic adaptations in response to NKL54 or SAHA treatment in TP53 mutated CRC PDOs. A. Heatmap showing the expression levels of the different zinc-dependent HDACs in the two PDOs, as indicated. The scale bar indicates the variance stabilizing transformed counts. The three independent biological replicates are shown. PDOs were treated for 6 hours with NKL54 [10 μM] or SAHA [5 μM]. B. Box plots showing expression levels (TPM) of genes up or downregulated in response to HDACIs for PDO19 (left) and PDO71 (right). Genes are considered differentially expressed with an absolute $\log_2$ (fold change) > 1 and adjusted p value < 0.05. C. Venn diagrams showing the number of genes commonly and exclusively upregulated in the two PDOs in response to SAHA (top) and NKL54 (bottom). D. Venn diagrams showing the number of genes commonly and exclusively upregulated by the two HDACIs in PDO19 (left) and PDO71 (right). E. Comparative analysis of the increased expression of the genes commonly upregulated by NKL54 and SAHA (compared to untreated) in the two PDOs as indicated. F. Scatter plots displaying expression log2(fold change) in response to SAHA (x axis) and NKL54 (y axis) for all detected genes (grey dots). The commonly upregulated genes are highlighted in pink. In most cases the upregulation is more substantial in SAHA-treated PDOs. G. Bar plot of the most significantly enriched functional terms according to the Gene Ontology (GO): Biological Process, (BP), Molecular Function (MF) and Cellular Component (CC), Reactome or KEGG databases. Genes commonly upregulated in response to SAHA or NKL54 treatment in both PDOs were analyzed. The top terms for each functional database are shown. Terms and pathways are considered significant with p value < 0.05. H. Bar plot as in (G) with genes upregulated in response to SAHA in the two PDOs were analyzed. The top terms for each functional database are shown, I. Bar plot as in (H) with NKL54 instead of SAHA.

Finally, cluster 4 groups TSS with reduced chromatin accessibility, corresponding to genes that show the lowest level of expression (Fig. 5A and B) and comprise the GO categories olfactory receptor activity and intermediate filaments (Table S14). In the two PDOs analyzed, treatment with the HDACIs does not provoke overt modifications in the distribution of clusters.

Next, we analyzed the differentially accessible sites. This analysis was limited to SAHA treatment, since NKL54 treatment did not show evidence for differences compared to DMSO treated PDOs (Fig. S3B). Overall, 5843 peaks were differentially accessible after SAHA treatment of which 3193 were more and 2650 less accessible. The heatmap in Fig. 6A shows that increased accessibility, in response to SAHA, occurs in region poorly accessible, whereas reduced accessibility is observed mainly in region with more open chromatin. These results confirm the RNA-seq analysis, with a repression of abundantly expressed genes and an increase in low expressed genes, as the consequence of HDACs inhibition (Fig. 3B). A similar behavior is observed in the two PDOs.

The genomic distribution of the ATAC-seq peaks was determined using ChIPseeker (Fig. 6B). In general, accessible regions in PDOs are mainly localized within gene bodies and promoters, as previously observed in other models [62–64]. The same genomic distribution is generally maintained in regions that show an increased accessibility after SAHA treatment. More specifically, we notice a redistribution of ATAC-seq signals within the promoter regions, with an enrichment of more distal regions from the TSS (Fig. 6B middle). In contrast, for genomic regions that have experienced a reduction in accessibility, we find more than half of the ATAC-seq signals in promoter regions (Fig. 6B right).

Finally, we applied computational analysis to search for enriched motifs that could predict TFs binding within the differentially accessible regions regulated by SAHA. For the more accessible chromatin regions the highest enriched transcription factors (TF) motifs were CTCF (CCCTC-binding factor) and FOS-AP1 (Fig. 6C). The enrichment for CTCF insulator protein binding motifs indicates that SAHA could influence gene boundaries and enhancers activities [65,66] eventually remodeling the topology of chromatin domains. For the less accessible regions, binding sites for members of the Kruppel-like factors (KLFs) family of TFs were the most highly enriched motifs (Fig. 6C).

3.8. Chromatin accessibility to pro-apoptotic and anti-apoptotic genes is differentially modulated by SAHA

SAHA treatment efficiently induced apoptosis in the two PDOs with mutations in *TP53*, possibly by regulating the expression of BCL2 family members (Fig. 4B). To better understand the effect of SAHA on cell death and chromatin accessibility, we analyzed the presence of differentially accessible ATAC-seq peaks in BCL2 family members whose mRNAs are modulated in response to SAHA. The pro-apoptotic BH3-only *BIK* and the anti-apoptotic *BCL2L1/BCLXL* are up- and downregulated, respectively, in both PDOs and show the appearance of distinct ATAC-seq peaks in response to SAHA treatment.

At steady-state, some individual differences in chromatin

accessibility can be observed between the two PDOs. In the case of *BIK*, chromatin accessibility increases in an intronic region (2nd intron) near the 3' end of the gene (Fig. 7A). This region may represent a putative enhancer. Analysis of ChIP-seq data obtained in the ENCODE project, showing enrichment of H3K27ac signals, and the possible presence of chromatin looping, confirmed that this region could represent an enhancer (Fig. S4). Motif discovery revealed a putative binding site for MZF1 (Fig. 7B), a zinc finger TF that has a dual function in CRC [67].

In *BCL2L1*, reduced chromatin accessibility is induced at multiple sites (n=3). The first and second regions are located within the second large intron, with the first region closest to the second exon (Fig. 7C). Data from ENCODE show that this intron contains multiple regions enriched in H3K27ac signals and the possible organization of chromatin looping, confirming the presence of putative enhancers (Fig. S5). Some of these H3K27ac domains correspond to the two regions that exhibit decreased chromatin accessibility in response to SAHA (1–2, Fig. 7C) The third region is located at the 3' end, downstream the third exon.

Motif discovery analysis in these regions (Fig. 7D) predicted with the highest score the binding sites of SPI1 and SP5, two transcription factors involved in tumorigenesis [67,68].

NKL54, which is unable to induce cell death, has no significant effect on chromatin accessibility at these loci in these two PDOs. In conclusion, induction of apoptosis and regulation of *BCL2L1* and *BIK* levels by SAHA correlate with modulation of chromatin accessibility at the relative genomic loci.

4. Discussion

PDOs obtained from CRC patients represent a new opportunity to evaluate drug effects and mechanisms of action in a more physiological 3D setting and under conditions that more closely resemble the patient's mutational profile [69]. For this manuscript, we generated and characterized PDOs from CRC patients to compare the efficacy of NKL54 and SAHA, two different HDACIs, with respect to the genomic mutational status. We have also defined changes in chromatin organization and transcriptional adaptations. PDOs carrying *TP53* mutations were selected, because they are common in CRC and arise late in the transition from adenoma to carcinoma, facilitating CRC progression, cancer stem cell expansion, and metastasis [70–73]. Patients with *TP53* mutations are associated with a higher death risk [74]. Therefore, exploring new therapeutic approaches using these PDO models is helpful to provide additional therapeutic interventions.

Analysis of WES revealed that the two PDOs have a specific pattern of mutations. In both PDOs, the RTK pathway is constitutively active because of mutations in *ERBB2*, *MAP2K1*, and *PTEN* in PDO19 and in *KRAS* in PDO71. *APC* is frequently mutated, albeit with a different pattern of mutations in all PDOs we have generated. As previously observed, these PDOs retain the mutation pattern of the primary tumor from which they originated [7]. However, WES analysis performed at different time points after the initial culture, indicates that subclone selection may be occurring in PDO71.

NKL54 is nearly ineffective in inducing cell death in these two PDOs.
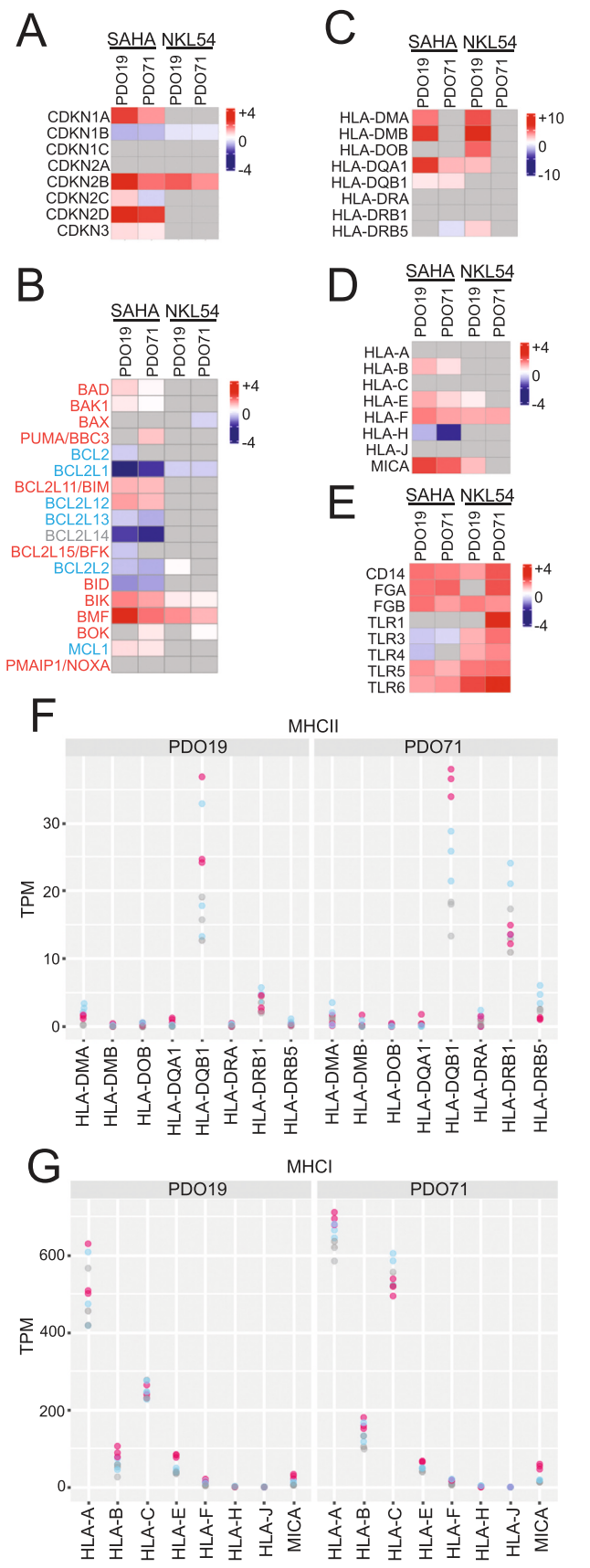
Fig. 4. Regulation of CDKIs, BCL2 family members and MHC genes in response to HDACIs. A. Heatmap reporting the expression levels (log2 fold change relative to untreated cells) of the indicated CDKIs family members in response to 6 hours of treatment with SAHA or NKL54 in the two PDOs, as indicated. Positive $\log_2$ fold change is indicated in red, negative in blue, as indicated in the scale bar. Genes that are not differentially expressed in a sample are indicated in grey. B. Same as panel A, showing BCL2 family members. Pro-apoptotic family members are in red, anti-apoptotic in light blue and genes with debated function in gray. C. Same as panel A, showing MHC class II genes. D. Same as panel A, showing MHC class I genes, E. Same as panel A, showing some genes of the Reactome category "diseases of the immune system". F. Class II MHC genes expression in PDOs treated with SAHA (pink), NKL54 (light blue), or untreated (grey) for 6 hours as indicated. Expression values are shown in TPM, each dot represents a replicate. G. Like (F), but for class I MHC genes.

In a previous study in 2D cancer cell lines, NKL54 was able to induce histone acetylation and apoptosis, though less efficiently than SAHA [23]. We confirmed that NKL54 can suppress cell proliferation at a concentration of 5 μM in CRC cell lines grown in a 2D culture. Therefore, PDOs represent a more resistant model for cellular stress that ultimately triggers cell death, and thus more closely resemble the patient's condition. At present, it is unclear whether the lower efficacy of NKL54 is due to a different uptake of the compound or a lower responsiveness of these two PDOs. Although off-targets for SAHA have recently been identified [46], the comparative analysis of a group of genes that are commonly upregulated by the two HDACIs in the two PDOs, suggests that SAHA is more efficient than NKL54 in inhibiting class I HDACs in CRC PDOs.

We confirmed that HDACIs have opposite effects on genes with high and low expression levels [23,48]. In fact, we see upregulation for genes with low expression, whereas highly expressed genes are repressed, an observation confirmed at the level of chromatin accessibility. In fact, in response to SAHA, cells open chromatin in relatively poorly accessible regions and, in contrast, decrease accessibility in well-accessible regions.

As observed previously, the effect of HDACIs manifests in already accessible regions, even if characterized by a relatively low signal, rather than opening new regions [62]. These regions are enriched for CTCF and FOS/AP1 binding motifs. Interestingly, in cutaneous T-cell lymphoma, the presence of the CTCF pattern or the absence of the AP1 pattern are both predictive of patient response to treatment with HDACIs [62].

Immunomodulation and immunotherapy enhancement are novel activities triggered by inhibition of HDACs. [75–77]. Many MHC class I and class II genes are upregulated in CRC cell lines in response to various HDACIs. [44,77–80]. We confirmed that some MHC class I and class II are upregulated in response to HDACIs, in the two PDOs studied. However, this response also shows patient selectivity, and interestingly, NKL54 and SAHA have a comparable effect on MHC class II genes. It is important to note that MHC class II genes are expressed at very low levels in both PDOs, and the strongest effect is exerted on *HLA-DMA* and *HLA-DMB* genes. The encoded proteins catalyze the exchange and loading of peptides onto MHC II molecules [81].

The efficacy of NKL54 in enhancing MHC gene expression was confirmed by functional analysis. Both inhibitors also enhanced the expression of various innate immunity genes [62,82]. This is another case where NKL54 was more effective compared to SAHA.

Members of the BCL2 family are key regulators of the intrinsic/mitochondrial pathway of apoptosis [83] SAHA efficiently triggers apoptosis in both PDOs, by regulating the expression of several BCL2 family members [43,84]. In particular, it strongly suppressed the expression of the anti-apoptotic *BCL2L1*. NKL54 was much less effective in upregulating *BIK* and *BMF* and did not repress *BCL2L1* expression. These shortcomings may explain its failure to induce apoptosis.

BCL2L1 is frequently overexpressed in CRC, is critical for the progression of adenoma carcinoma, and has drawn attention to the use of specific inhibitors [85–87]. ATAC-seq analysis identified three regions in *BCL2L1* where accessibility decreased after SAHA treatment. These
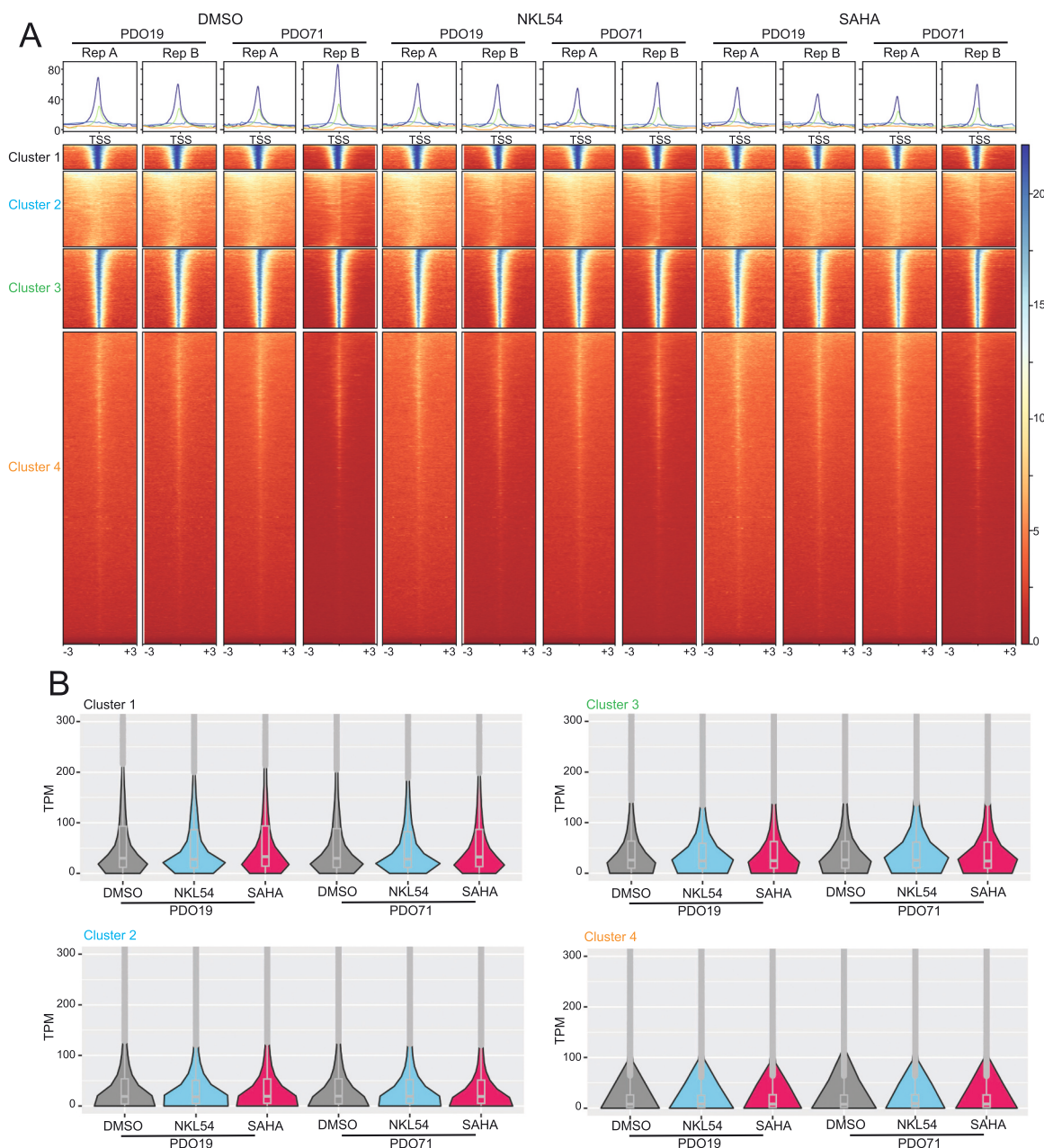
Fig. 5. DNA accessibility and gene expression. A. Profiles (top) and heatmaps (bottom) depicting ATAC-seq-normalized enrichment with the center TSS of two replicates for each condition. PDOs were treated with NKL54 (10 μM) or SAHA (5 μM) for 6 hours. Genomic loci (heatmap lines) are divided into four clusters based on enrichment in the four control samples (DMSO) and ordered by degree of enrichment within each cluster. The cluster sizes are as follows: Cluster 1, 2176 genes; Cluster 2, 6341 genes; Cluster 3, 7035 genes; Cluster 4, 11915 genes. A region extending 3Kb upstream and downstream from TSS is analyzed. In the heat maps, blue indicates high enrichment, red low. The colors of the profile lines indicate the four clusters. B. Violin plots illustrating the expression levels (TPM) of genes belonging to the four different clusters defined in (A). Expression data are from PDOs treated with NKL54 (10 μM) or SAHA (5 μM) for 6 hours.

regions are located within the intron 2 and at the 3' end of the gene. Motif discovery identified SP5 as the most enriched motif in two of these regions. Of note, SP5 is a target and effector of the WNT/β-catenin pathway [88–90]. Clearly, additional mechanisms could operate to control *BCL2L1* transcription. In cultured cell lines, ATF3 was reported to be engaged by HDACIs to repress *BCL2L1* after binding to its promoter [91]. Further studies will be required to demonstrate the role of SP5 in regulating *BCL2L1* expression.

In summary, our results suggest usage of HDACIs in combination with BCL2L1 inhibitors to efficiently induce cell death in CRC cells [92].

5. Conclusions

Epigenetic therapies in solid cancers, including the use of HDACIs, are currently being investigated to both target cancer cells and modulate the tumor microenvironment. The strategy is to enhance the effect of immunotherapy [77]. Our studies with two PDOs provide further evidence for the action of HDACIs as transcriptional modulators of key regulators of the cell cycle, apoptosis, and the immune response in CRC in the context of defective TP53. The ATAC-seq data shed lights on alterations in chromatin accessibility of genes that play a key role in the aggressiveness and therapy resistance of CRC, such as *BCL2L1*. Furthermore, although our exploratory study needs to be validated in a larger cohort of PDOs, we have uncovered patient-specific differences in
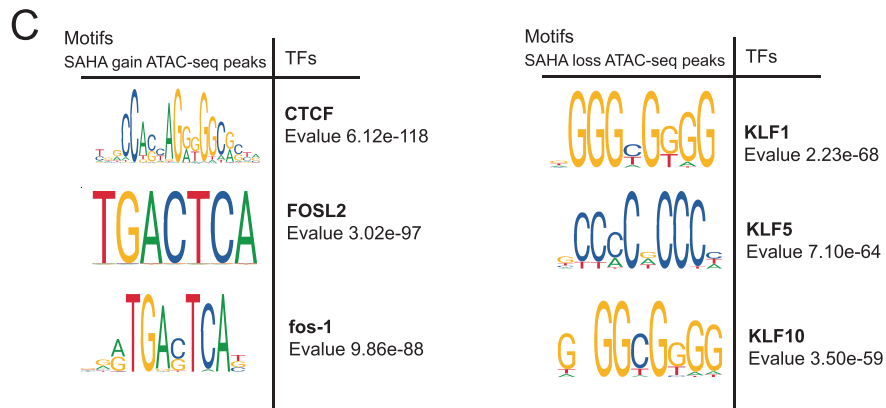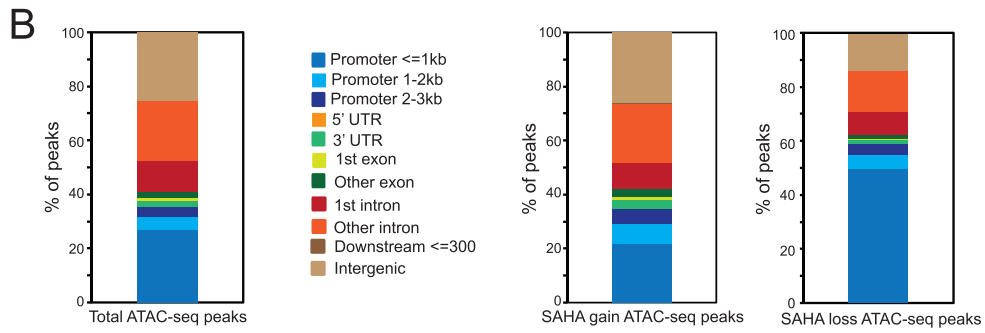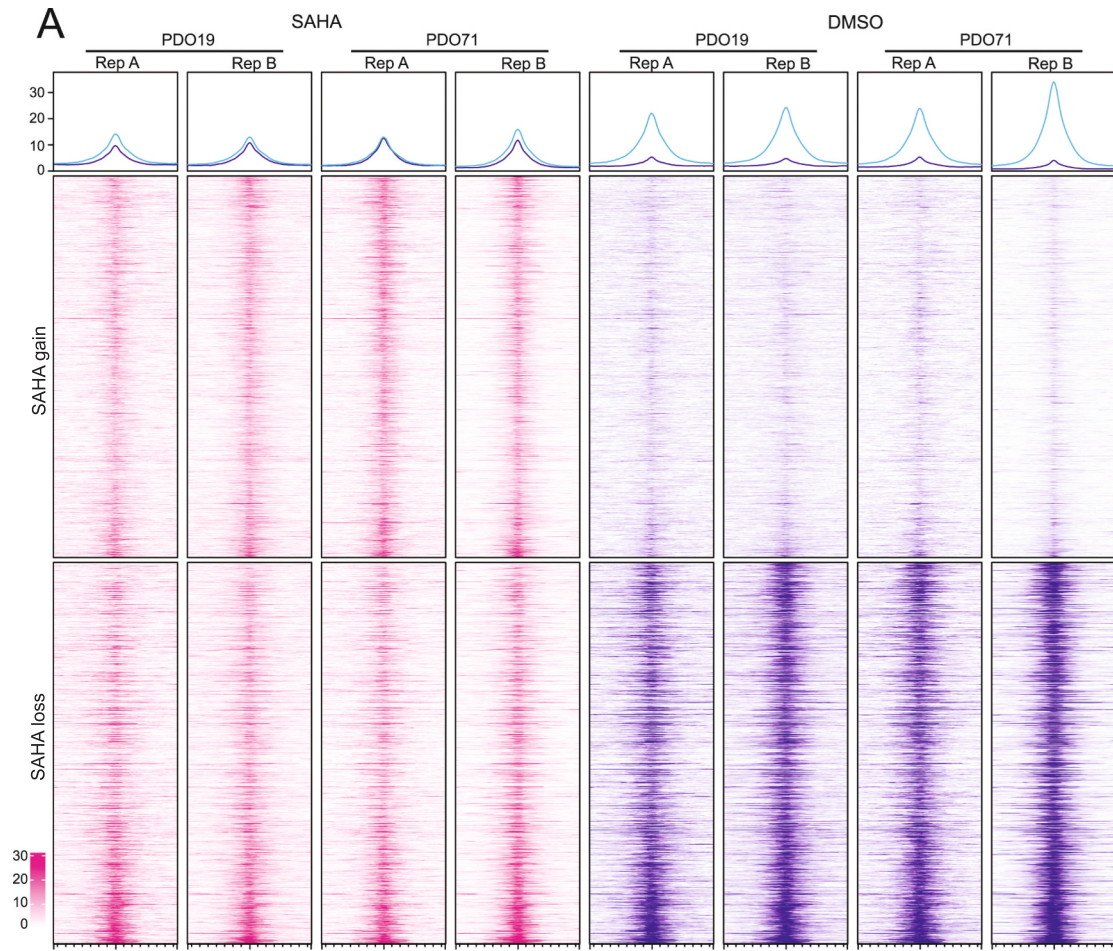
(caption on next page)

Fig. 6. Differentially accessible genomic regions in response to HDACIs. A. Profiles (top) and heatmaps (bottom) depicting ATAC-seq-normalized enrichment of a region extending 1.5 Kb upstream and downstream from the center of the peak. Two replicates per condition are shown: Treatment with SAHA [5 μM] for 6 hours (pink) and DMSO controls (purple). In the heatmap, darker color indicates higher enrichment. Two groups of genomic regions are shown as results of differential enrichment analysis: SAHA gain (top) and SAHA loss (bottom). In the profiles, enrichment of SAHA gain regions is indicated by the purple line (higher in SAHA than in DMSO samples), and enrichment of SAHA loss regions is indicated by the light blue line (lower in SAHA than in DMSO samples). SAHA gain are regions with significantly higher enrichment in SAHA-treated samples, SAHA loss are regions where enrichment is significantly higher in control/DMSO samples. B. Column plot showing the annotation of the genomic regions of the total consensus peaks (%) used to perform the differential enrichment analysis (left). Middle and right, column plots showing the annotation of the genomic regions of the SAHA gain and SAHA loss peak lists. C. The top three motifs enriched in the SAHA gain (left) and SAHA loss (right) regions. The name of the motif-binding protein and E value are indicated.
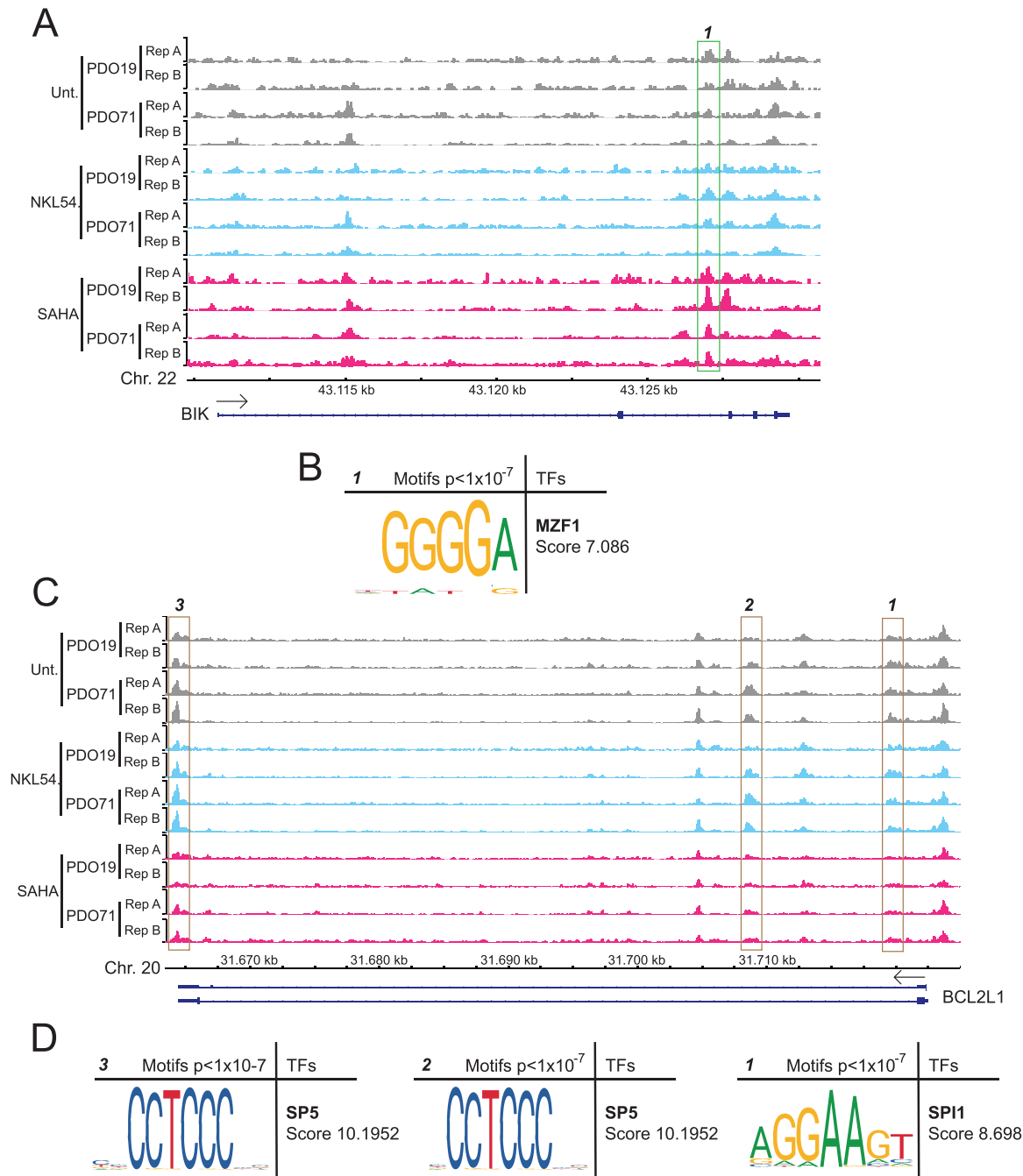

Fig. 7. Examples of genomic accessibility regions changing upon HDACI treatment. A. Integrative Genomics Viewer visualization of normalized ATAC-seq tracks of *BIK* gene region. Each track represents a replicate of the two PDOs untreated (grey) or treated with NKL54 (light blue) or SAHA (pink). The green box highlights the differentially enriched genomic region. B. Top motif matched to the differentially enriched genomic region indicated in A., with the binding protein name and score. C. Integrative Genomics Viewer visualization of normalized ATAC-seq tracks of *BCL2L1* gene region. Each track represents a replicate of the two PDOs untreated (grey) or treated with NKL54 (light blue) or SAHA (pink). The brown boxes highlight the differentially enriched genomic regions. D. Top motifs matched to the differentially enriched genomic regions indicated in C., with the binding protein names and scores.

the ability of HDACIs to modulate *HLA* genes. This is an important aspect to better understand the use of these inhibitors in combination with immunotherapy. In summary, PDOs are useful models to test the potency and efficacy of HDACIs and to validate new and more effective epigenetic drugs.

Funding

CRediT authorship contribution statement

Teresa Gagliano: Writing – original draft, Visualization, Validation, Methodology, Investigation, Formal analysis, Data curation. **Giovanni Terrosu:** Resources. **Claudio Brancolini:** Writing – original draft, Visualization, Supervision, Project administration, Funding acquisition, Data curation, Conceptualization. **Vittorio Cherchi:** Resources. **Emiliano Dalla:** Writing – original draft, Formal analysis, Data curation. **Christian X Weichenberger:** Writing – original draft, Formal analysis, Data curation. **Martina Minisini:** Resources. **Eros Di Giorgio:** Resources. **Emanuela Kerschbamer:** Writing – original draft, Visualization, Validation, Methodology, Investigation, Formal analysis, Data curation. **Umberto Baccarani:** Resources.

Declaration of Competing Interest

The authors declare that they have no known competing financial interests or personal relationships that could have appeared to influence the work reported in this paper.

Data accessibility

RNA-seq and ATAC-seq data have been deposited in NCBI's Gene Expression Omnibus and are accessible through GEO. Series https://www.ncbi.nlm.nih.gov/geo/query/acc.cgi?acc=GSE246046.

Acknowledgements

Appendix A. Supporting information

Supplementary data associated with this article can be found in the online version at doi:10.1016/j.biopha.2024.116374.

References

[1] D. Hanahan, Hallmarks of cancer: new dimensions, Cancer Discov. 12 (2022) 31–46.

[2] N. McGranahan, C. Swanton, Clonal heterogeneity and tumor evolution: past, present, and the future, Cell 168 (2017) 613–628.

[3] D. Yang, M.G. Jones, S. Naranjo, W.M. Rideout 3rd, K.H.J. Min, R. Ho, W. Wu, J. M. Replogle, J.L. Page, J.J. Quinn, et al., Lineage tracing reveals the phylodynamics, plasticity, and paths of tumor evolution, Cell 185 (2022), 1905-1923.e25.

[4] H. Sung, J. Ferlay, R.L. Siegel, M. Laversanne, I. Soerjomataram, A. Jemal, F. Bray, Global Cancer Statistics 2020: GLOBOCAN Estimates of Incidence and Mortality Worldwide for 36 Cancers in 185 Countries, CA Cancer J. Clin. 71 (2021) 209–249.

[5] S. Vodenkova, T. Buchler, K. Cervena, V. Veskrnova, P. Vodicka, V. Vymetalkova, 5-fluorouracil and other fluoropyrimidines in colorectal cancer: Past, present and future, Pharm. Ther. 206 (2020) 107447.

[6] F. Papaccio, B. García-Mico, F. Gimeno-Valiente, M. Cabeza-Segura, V. Gambardella, M.F. Gutiérrez-Bravo, C. Alfaro-Cervelló, C. Martinez-Ciarpaglini, P. Rentero-Garrido, S. Zúñiga-Trejos, et al., Proteotranscriptomic analysis of advanced colorectal cancer patient derived organoids for drug sensitivity prediction, J. Exp. Clin. Cancer Res 42 (2023) 8.

[7] M. van de Wetering, H.E. Francies, J.M. Francis, G. Bounova, F. Iorio, A. Pronk, W. van Houdt, J. van Gorp, A. Taylor-Weiner, L. Kester, et al., Prospective derivation of a living organoid biobank of colorectal cancer patients, Cell 161 (2015) 933–945.

[8] C. Marx, J. Sonnemann, M. Beyer, O.D.K. Maddocks, S. Lilla, I. Hauzenberger, A. Piée-Staffa, K. Siniuk, S. Nunna, L. Marx-Blümel, et al., Mechanistic insights into p53-regulated cytotoxicity of combined entinostat and irinotecan against colorectal cancer cells, Mol. Oncol. 15 (2021) 3404–3429.

[9] M. Jian, L. Ren, G. He, Q. Lin, W. Tang, Y. Chen, J. Chen, T. Liu, M. Ji, Y. Wei, et al., A novel patient-derived organoids-based xenografts model for preclinical drug response testing in patients with colorectal liver metastases, J. Transl. Med 18 (2020) 234.

[10] M. Hendrych, K. Říhová, B. Adamová, V. Hradil, M. Stiborek, P. Vlček, M. Hermanová, J. Vašíčková, P. Beneš, J. Šmarda, et al., Disulfiram increases the efficacy of 5-fluorouracil in organotypic cultures of colorectal carcinoma, Biomed. Pharm. 153 (2022) 113465.

[11] Y. Yao, X. Xu, L. Yang, J. Zhu, J. Wan, L. Shen, F. Xia, G. Fu, Y. Deng, M. Pan, et al., Patient-derived organoids predict chemoradiation responses of locally advanced rectal cancer, Cell Stem Cell 26 (2020) 17–26.e6.

[12] K. Palamaris, M. Moutafi, H. Gakiopoulou, S. Theocharis, Histone Deacetylase (HDAC) Inhibitors: A Promising Weapon to Tackle Therapy Resistance in Melanoma, Int J. Mol. Sci. 23 (2022) 3660.

[13] D. Singh, M.A. Khan, H.R. Siddique, Role of epigenetic drugs in sensitizing cancers to anticancer therapies: emerging trends and clinical advancements, Epigenomics 15 (2023) 517–537.

[14] E. Seto, M. Yoshida, Erasers of histone acetylation: the histone deacetylase enzymes, Cold Spring Harb. Perspect. Biol. 6 (2014) a018713.

[15] C. Brancolini, T. Gagliano, M. Minisini, HDACs and the epigenetic plasticity of cancer cells: Target the complexity, Pharm. Ther. 238 (2022) 108190.

[16] T.C.S. Ho, A.H.Y. Chan, A. Ganesan, Thirty Years of HDAC Inhibitors: 2020 Insight and Hindsight, J. Med Chem. 63 (2020) 2460–12484.

[17] J. Melesina, C.V. Simoben, L. Praetorius, E.F. Bülbül, D. Robaa, W. Sippl, Strategies to design selective histone deacetylase inhibitors, ChemMedChem 16 (2021) 1336–1359.

[18] D. Karagiannis, T. Rampias, HDAC inhibitors: dissecting mechanisms of action to counter tumor heterogeneity, Cancers (Basel) 13 (2021) 3575.

[19] A.D. Bondarev, M.M. Attwood, J. Jonsson, V.N. Chubarev, V.V. Tarasov, H. B. Schiöth, Recent developments of HDAC inhibitors: Emerging indications and novel molecules, Br. J. Clin. Pharm. 87 (2021) 4577–4597.

[20] J.L. Guerriero, A. Sotayo, H.E. Ponichtera, J.A. Castrillon, A.L. Pourzia, S. Schad, S. F. Johnson, R.D. Carrasco, S. Lazo, R.T. Bronson, et al., Class IIa HDAC inhibition reduces breast tumours and metastases through anti-tumour macrophages, Nature 543 (2017) 428–432.

[21] Z. Lu, J. Zou, S. Li, M.J. Topper, Y. Tao, H. Zhang, X. Jiao, W. Xie, X. Kong, M. Vaz, H. Li, et al., Epigenetic therapy inhibits metastases by disrupting premetastatic niches, Nature 579 (2020) 284–290.

[22] T. Gagliano, K. Shah, S. Gargani, L. Lao, M. Alsaleem, J. Chen, V. Ntafis, P. Huang, A. Ditsiou, V. Vella, et al., PIK3Cδ expression by fibroblasts promotes triple-negative breast cancer progression, J. Clin. Invest 130 (2020) 3188–3204.

[23] M. Minisini, E. Di Giorgio, E. Kerschbamer, E. Dalla, M. Faggiani, E. Franforte, F. J. Meyer-Almes, R. Ragno, L. Antonini, A. Mai, et al., Transcriptomic and genomic studies classify NKL54 as a histone deacetylase inhibitor with indirect influence on MEF2-dependent transcription, Nucleic Acids Res 50 (2022) 2566–2586.

[24] P. Ewels, M. Magnusson, S. Lundin, M. Käller, MultiQC: summarize analysis results for multiple tools and samples in a single report, Bioinformatics 32 (2016) 3047–3048.

[25] H. Li, B. Handsaker, A. Wysoker, T. Fennell, J. Ruan, N. Homer, G. Marth, G. Abecasis, R. Durbin, 1000 Genome Project Data Processing Subgroup, The Sequence Alignment/Map format and SAMtools, Bioinformatics 25 (2009) 2078–2079.

[26] K. Cibulskis, M.S. Lawrence, S.L. Carter, A. Sivachenko, D. Jaffe, C. Sougnez, S. Gabriel, M. Meyerson, E.S. Lander, G. Getz, Sensitive detection of somatic point mutations in impure and heterogeneous cancer samples, Nat. Biotechnol. 31 (2013) 213–219.

[27] P. Danecek, J.K. Bonfield, J. Liddle, J. Marshall, V. Ohan, M.O. Pollard, A. Whitwham, T. Keane, S.A. McCarthy, R.M. Davies, et al., Twelve years of SAMtools and BCFtools, Gigascience 10 (2021) giab008.

[28] F. Manders, A.M. Brandsma, J. de Kanter, M. Verheul, R. Oka, M.J. van Roosmalen, B. van der Roest, A. van Hoeck, E. Cuppen, R. van Boxtel, MutationalPatterns: the one stop shop for the analysis of mutational processes, BMC Genom. 23 (2022) 134.

[29] M.I. Love, C. Soneson, P.F. Hickey, L.K. Johnson, N.T. Pierce, L. Shepherd, M. Morgan, R. Patro, Tximeta: Reference sequence checksums for provenance identification in RNA-seq, PLoS Comput. Biol. 16 (2020) e1007664.

[30] J. Rainer, L. Gatto, C.X. Weichenberger, ensembldb: an R package to create and use Ensembl-based annotation resources, Bioinformatics 17 (2019) 3151–3153.

[31] T. Wu, E. Hu, S. Xu, M. Chen, P. Guo, Z. Dai, T. Feng, L. Zhou, W. Tang, L. Zhan, et al., clusterProfiler 4.0: A universal enrichment tool for interpreting omics data, Innov. (Camb.) 12 (2021) 100141.

[32] P.A. Ewels, A. Peltzer, S. Fillinger, H. Patel, J. Alneberg, A. Wilm, M.U. Garcia, P. Di Tommaso, S. Nahnsen, The nf-core framework for community-curated bioinformatics pipelines, Nat. Biotechnol. 38 (2020) 276–278.

[33] F. Ramírez, D.P. Ryan, B. Grüning, V. Bhardwaj, F. Kilpert, A.S. Richter, S. Heyne, F. Dündar, T. Manke, deepTools2: a next generation web server for deep-sequencing data analysis 2016 Jul 8 44 (W1) (2016) W160–W165.

[34] Q. Wang, M. Li, T. Wu, L. Zhan, L. Li, M. Chen, W. Xie, Z. Xie, E. Hu, S. Xu, et al., Exploring Epigenomic Datasets by ChIPseeker (2022), Curr. Protoc. 2 (2022) e585.

[35] T.L. Bailey, J. Johnson, C.E. Grant, W.S. Noble, The MEME Suite, Nucleic Acids Res 43 (2015) W39–W49.

[36] J.A. Castro-Mondragon, R. Riudavets-Puig, I. Rauluseviciute, R.B. Lemma, L. Turchi, R. Blanc-Mathieu, J. Lucas, P. Boddie, A. Khan, N. Manosalva Pérez, J. A. Castro-Mondragon, R. Riudavets-Puig, I. Rauluseviciute, R.B. Lemma, L. Turchi, R. Blanc-Mathieu, J. Lucas, P. Boddie, A. Khan, N. Manosalva Pérez, Nucleic Acids Res 50 (2022) D165–D173.

[37] S. Domcke, R. Sinha, D.A. Levine, C. Sander, N. Schultz, Evaluating cell lines as tumour models by comparison of genomic profiles, Nat. Commun. 4 (2013) 2126.

[38] A. Russo, V. Bazan, B. Iacopetta, D. Kerr, T. Soussi, N. Gebbia, TP53-CRC Collaborative Study Group, The TP53 colorectal cancer international collaborative study on the prognostic and predictive significance of p53 mutation: influence of tumor site, type of mutation, and adjuvant treatment, J. Clin. Oncol. 23 (2005) 7518–7528.

[39] H. Elsaleh, B. Powell, K. McCaul, F. Grieu, R. Grant, D. Joseph, B. Iacopetta, P53 alteration and microsatellite instability have predictive value for survival benefit from chemotherapy in stage III colorectal carcinoma, Clin. Cancer Res. 7 (2001) 1343–1349.

[40] S.H. Zaidi, T.A. Harrison, A.I. Phipps, R. Steinfelder, Q.M. Trinh, C. Qu, B. L. Banbury, P. Georgeson, C.S. Grasso, M. Giannakis, Nat. Commun. 11 (2020) 3644.

[41] O. Zajac, J. Raingeaud, F. Libanje, C. Lefebvre, D. Sabino, I. Martins, P. Roy, C. Benatar, C. Canet-Jourdan, P. Azorin, Tumour spheres with inverted polarity drive the formation of peritoneal metastases in patients with hypermethylated colorectal carcinomas, Nat. Cell Biol. 20 (2018) 296–306.

[42] K.C. Hicks, P.L. Chariou, Y. Ozawa, C.M. Minnar, K.M. Knudson, T.J. Meyer, J. Bian, M. Cam, J. Schlom, S.R. Gameiro, Tumour-targeted interleukin-12 and entinostat combination therapy improves cancer survival by reprogramming the tumour immune cell landscape, Nat. commun. 12 (2021) 5151.

[43] Jenkins L.J., Luk I.Y., Fairlie W.D., Lee E.F., Palmieri M., Schoffer K.L., Tan T., Ng I., Vukelic N., Tran S. et al. (2023) Genotype-Tailored ERK/MAPK Pathway and HDAC Inhibition Rewires the Apoptotic Rheostat to Trigger Colorectal Cancer Cell Death Mol Cancer Ther 22, 52-62.

[44] W. Blaszczak, G. Liu, H. Zhu, W. Barczak, A. Shrestha, G. Albayrak, S. Zheng, D. Kerr, A. Samsonova, N.B. La Thangue, Immune modulation underpins the anti-cancer activity of HDAC inhibitors, Mol. Oncol. 15 (2021) 3280–3298.

[45] Y. Kawamura, L. Hua, A. Gurtner, E. Wong, J. Kiyokawa, N. Shah, J. Gorham, H. Wakimoto, S.D. Rabkin, et al., Histone deacetylase inhibitors enhance oncolytic herpes simplex virus therapy for malignant meningioma, Biomed. Pharmacother. 155 (2022) 113843.

[46] S. Lechner, M.I.P. Malgapo, C. Grätz, R.R. Steimbach, A. Baron, P. Rüther, S. Nadal, C. Stumpf, C. Loos, X. Ku, et al., Target deconvolution of HDAC pharmacopoeia reveals MBLAC2 as common off-target, Nat. Chem. Biol. 18 (2022) 812–820.

[47] E.D. Salmon, S.L. Shaw, J.C. Waters, C.M. Waterman-Storer, P.S. Maddox, E. Yeh, K. Bloom, A high-resolution multimode digital microscope system, Methods Cell Biol. 114 (2013) 179–210.

[48] C.L. Lamparter, L.M. Winn, Valproic acid exposure decreases Cbp/p300 protein expression and histone acetyltransferase activity in P19 cells, Toxicol. Appl. Pharm. 306 (2016) 69–78.

[49] Y. Koriyama, K. Sugitani, K. Ogai, S. Kato, Neuritogenic activity of trichostatin A in adult rat retinal ganglion cells through acetylation of histone H3 lysine 9 and RARβ induction, J. Pharm. Sci. 124 (2014) 112–116.

[50] K. Meganathan, S. Jagtap, S.P. Srinivasan, V. Wagh, J. Hescheler, J. Hengstler, M. Leist, A. Sachinidis, Neuronal developmental gene and miRNA signatures induced by histone deacetylase inhibitors in human embryonic stem cells, Cell Death Dis. 6 (2015) e1756.

[51] C. Henderson, C. Brancolini, Apoptotic pathways activated by histone deacetylase inhibitors: implications for the drug-resistant phenotype, Drug Resist Updat 6 (2003) 247–256.

[52] A. Newbold, K.J. Falkenberg, H.M. Prince, R.W. Johnstone, How do tumor cells respond to HDAC inhibition? FEBS J. 283 (2016) 4032–4046.

[53] T. Hitomi, Y. Matsuzaki, T. Yokota, Y. Takaoka, T. Sakai, p15(INK4b) in HDAC inhibitor-induced growth arrest, FEBS Lett. 554 (2003) 347–350.

[54] T. Yokota, Y. Matsuzaki, K. Miyazawa, F. Zindy, M.F. Roussel, T. Sakai, Histone deacetylase inhibitors activate INK4d gene through Sp1 site in its promoter, Oncogene 23 (2004) 5340–5349.

[55] M. Gialitakis, A. Kretsovali, C. Spilianakis, L. Kravariti, J. Mages, R. Hoffmann, A. K. Hatzopoulos, J. Papamatheakis, Coordinated changes of histone modifications and HDAC mobilization regulate the induction of MHC class II genes by Trichostatin A, Nucleic Acids Res 34 (2006) 765–772.

[56] S.D. Puvvada, H. Li, L.M. Rimsza, S.H. Bernstein, R.I. Fisher, M. LeBlanc, M. Schmelz, B. Glinsmann-Gibson, T.P. Miller, et al., Maddox AM, A phase II study of belinostat (PXD101) in relapsed and refractory aggressive B-cell lymphomas: SWOG S0520, Leuk. Lymphoma 57 (2016) 2359–2369.

[57] J. Bae, T. Hideshima, Y.T. Tai, Y. Song, P. Richardson, N. Raje, N.C. Munshi, K. C. Anderson, Histone deacetylase (HDAC) inhibitor ACY241 enhances anti-tumor activities of antigen-specific central memory cytotoxic T lymphocytes against multiple myeloma and solid tumors, Leukemia 32 (2018) 1932–1947.

[58] R.B. Baleeiro, C.J. Bouwens, P. Liu, C. Di Gioia, L.S.C. Dunmall, A. Nagano, R. Gangeswaran, C. Chelala, H.M. Kocher, N.R. Lemoine, Y. Wang, MHC class II molecules on pancreatic cancer cells indicate a potential for neo-antigen-based immunotherapy, Oncoimmunology 11 (2022) 2080329.

[59] M. Koyama, G.R. Hill, The primacy of gastrointestinal tract antigen-presenting cells in lethal graft-versus-host disease, Blood 134 (2019) 2139–2148.

[60] L. Iuliano, E. Dalla, R. Picco, S. Mallavarapu, M. Minisini, E. Malavasi, C. Brancolini, Proteotoxic stress-induced apoptosis in cancer cells: understanding the susceptibility and enhancing the potency, Cell Death Discov. 8 (2022) 407.

[61] S. Ishihara, Y. Sasagawa, T. Kameda, H. Yamashita, M. Umeda, N. Kotomura, M. Abe, Y. Shimono, I. Nikaido, Local states of chromatin compaction at transcription start sites control transcription levels, Nucleic Acids Res 49 (2021) 8007–8023.

[62] K. Qu, L.C. Zaba, A.T. Satpathy, P.G. Giresi, R. Li, Y. Jin, R. Armstrong, C. Jin, N. Schmitt, Z. Rahbar, et al., Chromatin Accessibility Landscape of Cutaneous T Cell Lymphoma and Dynamic Response to HDAC Inhibitors, Cancer Cell 32 (2017) 27–41.

[63] J. Li, D. Witonsky, E. Sprague, D. Alleyne, M.C. Bielski, K.M. Lawrence, S.S. Kupfer, Genomic and epigenomic active vitamin D responses in human colonic organoids, Physiol. Genom. 53 (2021) 235–248.

[64] P.O. Estève, U.S. Vishnu, H.G. Chin, S. Pradhan, Visualization and Sequencing of Accessible Chromatin Reveals Cell Cycle and Post-HDAC inhibitor Treatment Dynamics, J. Mol. Biol. 432 (2020) 5304–5321.

[65] J.R. Dixon, S. Selvaraj, F. Yue, A. Kim, Y. Li, Y. Shen, M. Hu, J.S. Liu, B. Ren, Topological domains in mammalian genomes identified by analysis of chromatin interactions, Nature 485 (2012) 376–380.

[66] J.A. da Costa-Nunes, D. Noordermeer, TADs: Dynamic structures to create stable regulatory functions, Curr. Opin. Struct. Biol. 81 (2023) 102622.

[67] S. Liu, X. Sima, X. Liu, H. Chen, Zinc Finger Proteins: Functions and Mechanisms in Colon Cancer, Cancers (Basel) 14 (2022) 5242.

[68] S. Gregoricchio, L. Polit, M. Esposito, J. Berthelet, L. Delestré, E. Evanno, M. Diop, I. Gallais, H. Aleth, M. Poplineau, et al., HDAC1 and PRC2 mediate combinatorial control in SPI1/PU.1-dependent gene repression in murine erythroleukaemia, Nucleic Acids Res 50 (2022) 7938–7958.

[69] Farin H.F., Mosa M.H., Ndreshkjana B., Grebbin B.M., Ritter B., Menche C., Kennel K.B., Ziegler P.K., Szabó L., Bollrath J. et al. (2023) Colorectal Cancer Organoid-Stroma Biobank Allows Subtype-Specific Assessment of Individualized Therapy Responses Cancer Discov. 13, 2192-2221.

[70] T. Cooks, I.S. Pateras, O. Tarcic, H. Solomon, A.J. Schetter, S. Wilder, G. Lozano, E. Pikarsky, T. Forshew, N. Rosenfeld, et al., Mutant p53 prolongs NF-κB activation and promotes chronic inflammation and inflammation-associated colorectal cancer, Cancer Cell 23 (5) (2013) 634–646, 2013 May 13.

[71] M. Nakayama, E. Sakai, K. Echizen, Y. Yamada, H. Oshima, T.S. Han, R. Ohki, S. Fujii, A. Ochiai, S. Robine, et al., Intestinal cancer progression by mutant p53 through the acquisition of invasiveness associated with complex glandular formation, Oncogene 36 (2017) 5885–5896.

[72] H. Solomon, N. Dinowitz, I.S. Pateras, T. Cooks, Y. Shetzer, A. Molchadsky, M. Charni, S. Rabani, G. Koifman, O. Tarcic, et al., Mutant p53 gain of function underlies high expression levels of colorectal cancer stem cells markers, Oncogene 37 (2018) 1669–1684.

[73] K.C.G. Berg, T.H. Brunsell, A. Sveen, S. Alagaratnam, M. Bjørnslett, M. Hektoen, K. W. Brudvik, B.I. Røsok, B.A. Bjørnbeth, A. Nesbakken, et al., Genomic and prognostic heterogeneity among RAS/BRAFV600E/TP53 co-mutated resectable colorectal liver metastases, Mol. Oncol. 15 (2021) 830–845.

[74] R. Schulz-Heddergott, N. Stark, S.J. Edmunds, J. Li, L.C. Conradi, H. Bohnenberger, F. Ceteci, F.R. Greten, M. Dobbelstein, U.M. Moll, Therapeutic Ablation of Gain-of-Function Mutant p53 in Colorectal Cancer Inhibits Stat3-Mediated Tumor Growth and Invasion, Cancer Cell 34 (2018) 298–314.

[75] S. Gomez, T. Tabernacki, J. Kobyra, P. Roberts, K.B. Chiappinelli, Combining epigenetic and immune therapy to overcome cancer resistance, Semin Cancer Biol. 65 (2020) 99–113.

[76] A.O. Adeshakin, F.O. Adeshakin, D. Yan, X. Wan, Regulating Histone Deacetylase Signaling Pathways of Myeloid-Derived Suppressor Cells Enhanced T Cell-Based Immunotherapy, Front Immunol. 13 (2022) 781660.

[77] N.K. Sedky, A.A. Hamdan, S. Emad, A.L. Allam, M. Ali, M.F. Tolba, Insights into the therapeutic potential of histone deacetylase inhibitor/immunotherapy combination regimens in solid tumors, Clin. Transl. Oncol. 24 (2022) 1262–1273.

[78] G. Liu, W. Barczak, L.N. Lee, A. Shrestha, N.M. Provine, G. Albayrak, H. Zhu, C. Hutchings, P. Klenerman, N.B. La Thangue, The HDAC inhibitor zabadinostat is a systemic regulator of adaptive immunity, Commun. Biol. 6 (2023) 102.

[79] L. Ferrari de Andrade, S. Kumar, A.M. Luoma, Y. Ito, P.H. Alves da Silva, D. Pan, J. W. Pyrdol, C.H. Yoon, K.W. Wucherpfennig, Inhibition of MICA and MICB Shedding Elicits NK-Cell-Mediated Immunity against Tumors Resistant to Cytotoxic T Cells, Cancer Immunol. Res 8 (2020) 769–780.

[80] C. Jiménez, L. Moreno, M.F. Segura, Epigenetic therapies for neuroblastoma: immunogenicity awakens, Mol. Oncol. 17 (2023) 718–721.

[81] M. Álvaro-Benito, E. Morrison, F. Ebner, E.T. Abualrous, M. Urbicht, M. Wieczorek, C. Freund, Distinct editing functions of natural HLA-DM allotypes impact antigen presentation and CD4+ T cell activation, Cell Mol. Immunol. 17 (2020) 133–142.

[82] M. Medon, E. Vidacs, S.J. Vervoort, J. Li, M.R. Jenkins, K.M. Ramsbottom, J. A. Trapani, M.J. Smyth, P.K. Darcy, P.W. Atadja, et al., HDAC Inhibitor Panobinostat Engages Host Innate Immune Defenses to Promote the Tumoricidal Effects of Trastuzumab in HER2+ Tumors, Cancer Res 77 (2017) 2594–2606.

[83] D. Kaloni, S.T. Diepstraten, A. Strasser, G.L. Kelly, BCL-2 protein family: attractive targets for cancer therapy, Apoptosis 28 (2023) 20–38.

[84] J.E. Bolden, W. Shi, K. Jankowski, C.Y. Kan, L. Cluse, B.P. Martin, K.L. MacKenzie, G.K. Smyth, R.W. Johnstone, HDAC inhibitors induce tumor-cell-selective pro-apoptotic transcriptional responses, Cell Death Dis. 4 (2013) e519.

[85] S. Colak, C.D. Zimberlin, E. Fessler, L. Hogdal, P.R. Prasetyanti, C.M. Grandela, A. Letai, J.P. Medema, Decreased mitochondrial priming determines chemoresistance of colon cancer stem cells, Cell Death Differ. 21 (2014) 1170–1177.

[86] H. Zhang, J. Xue, P. Hessler, S.K. Tahir, J. Chen, S. Jin, A.J. Souers, J.D. Leverson, L.T. Lam, Genomic analysis and selective small molecule inhibition identifies BCL-X(L) as a critical survival factor in a subset of colorectal cancer, Mol. Cancer 14 (2015) 126.

[87] P. Ramesh, T.R.M. Lannagan, R. Jackstadt, L. Atencia Taboada, N. Lansu, P. Wirapati, S.R. van Hooff, D. Dekker, J. Pritchard, A.B. Kirov, et al., BCL-XL is crucial for progression through the adenoma-to-carcinoma sequence of colorectal cancer, Cell Death Differ. 28 (2021) 3282–3296.

[88] G. Weidinger, C.J. Thorpe, K. Wuennenberg-Stapleton, J. Ngai, R.T. Moon, The Sp1-related transcription factors sp5 and sp5-like act downstream of Wnt/beta-catenin signaling in mesoderm and neuroectoderm patterning, Curr. Biol. 15 (2005) 489–500.

[89] M.W. Kennedy, R.B. Chalamalasetty, S. Thomas, R.J. Garriock, P. Jailwala, T. P. Yamaguchi, Sp5 and Sp8 recruit β-catenin and Tcf1-Lef1 to select enhancers to activate Wnt target gene transcription, Proc. Natl. Acad. Sci. USA 113 (2016) 3545–3550.

[90] A.P. Azambuja, M. Simoes-Costa, A regulatory sub-circuit downstream of Wnt signaling controls developmental transitions in neural crest formation, PLoS Genet 17 (2021) e1009296.

[91] Chüeh A.C., Tse J.W.T., Dickinson M., Ioannidis P., Jenkins L., Togel L., Tan B., Luk I., Davalos-Salas M., Nightingale R. et al. (2017) ATF3 Repression of BCL-XL Determines Apoptotic Sensitivity to HDAC Inhibitors across Tumor Types Clin Cancer Res. 23, 5573-5584.

[92] Kehr S., Vogler M. (2021) It's time to die: BH3 mimetics in solid tumors Biochim Biophys Acta Mol Cell Res. 1868, 118987.

[93] J.M. Zahm, S. Baconnais, S. Monier, N. Bonnet, G. Bessède, P. Gambert, E. Puchelle, G. Lizard, Chronology of cellular alterations during 7-ketocholesterol-induced cell death on A7R5 rat smooth muscle cells: analysis by time lapse-video microscopy and conventional fluorescence microscopy, Cytom. A 52 (2003) 57–69.